ALMA MATER STUDIORUM
UNIVERSITÀ DI BOLOGNA

DOTTORATO DI RICERCA IN

SCIENZE BIOMEDICHE E NEUROMOTORIE

Ciclo 38

Settore Concorsuale: 05/H2 - ISTOLOGIA

Settore Scientifico Disciplinare: BIO/17 - ISTOLOGIA

ROLE OF PHOSPHOINOSITIDE-DEPENDENT SIGNALING AND OPTIMIZATION OF PDZD2 GENOME EDITING IN VITRO MODEL IN MYELODYSPLASTIC NEOPLASMS AND ACUTE MYELOID LEUKEMIA

Presentata da: Irene Casalin

Coordinatore Dottorato

Matilde Yung Follo

Supervisore

Matilde Yung Follo

Co-supervisore

Tullia Maraldi

Esame finale anno 2026

TABLE OF CONTENTS

0. ABSTRACT

Myelodysplastic Neoplasms (MDS) and Acute Myeloid Leukemia (AML) are hematologic malignancies marked by ineffective hematopoiesis, differentiation defects, and profound epigenetic dysregulation.These alterations drive disease heterogeneity and therapeutic resistance, emphasizing the need for mechanistic insights to guide new treatments.

In the first part of this study, we investigated the molecular effects of Azacitidine (AZA) and Venetoclax (VEN), alone and in combination, in high-risk MDS (HR-MDS) patients and AML cell lines. We identified a recurrent *BCL2* frameshift mutation at baseline, which may influence sensitivity to AZA+VEN through non-canonical mechanisms. Analyses of patient-derived hematopoietic cells suggested interplay between phosphoinositide-dependent signaling and apoptotic pathways, further confirmed in leukemic cell lines. In these models, AZA+VEN induced caspase-dependent apoptosis, modulated BCL2 family proteins, and altered PLC/PKC and AKT/GSK3 signaling pathways, providing novel insight into the molecular basis of response and resistance to this combination therapy.

The second part of the project focused on developing a CRISPR-Cas9 genome-editing platform to investigate PDZD2, a poorly characterized gene hypermethylated in nearly 90% of AML cases and proposed as an epigenetic regulator of hematopoiesis. Conducted at Dr. Figueroa's laboratory at the University of Miami, this work established targeted editing in HEK293 cells, introducing defined modifications at the PDZD2 locus—including an HA tag, a CASP3 cleavage-site mutation, and NLS alterations. Sequencing analyses revealed locus-dependent variability, with efficient homozygous knock-ins at the CASP3 site but lower HDR rates and instability for the HA and NLS modifications.

Together, these two complementary projects integrate translational and mechanistic perspectives. The AZA+VEN study elucidates adaptive signaling networks with direct therapeutic relevance, while the PDZD2 genome-editing platform provides a methodological foundation to dissect epigenetic regulators in hematopoiesis. Collectively, this work advances our understanding of the molecular and epigenetic mechanisms driving leukemic progression and treatment response.

1. INTRODUCTION

1.1. Hematopoiesis and Differentiation

Hematopoiesis is the highly regulated process by which all blood cells are generated and mature from hematopoietic stem cells (HSCs). These multipotent cells reside primarily in the bone marrow and sustain lifelong hematopoiesis through their dual capacity of self-renewal and multilineage differentiation into both myeloid and lymphoid lineages (Figure 1)(1).

During embryonic development, hematopoiesis occurs in a series of temporally and spatially distinct waves. The first “primitive” wave originates in the yolk sac and primarily generates nucleated erythrocytes and limited myeloid progenitors. This is followed by a “definitive” wave characterized by the endothelial-to-hematopoietic transition (EHT), which occurs within the aorta-gonad-mesonephros (AGM) region and gives rise to long-term repopulating HSCs capable of self-renewal and full lineage potential (2–5). These definitive HSCs subsequently migrate to the fetal liver, which serves as the principal hematopoietic organ during mid-gestation, before homing to the bone marrow, which becomes the primary site of hematopoiesis in postnatal and adult life (1,6–8). The functional output of HSCs is tightly modulated by a complex network of intrinsic transcriptional and epigenetic programs, as well as extrinsic signals derived from the specialized bone marrow microenvironment, known as the hematopoietic niche. This niche provides essential cues that regulate HSCs quiescence, proliferation, and lineage commitment in response to physiological demands or stress signals (1). Hematopoietic differentiation proceeds through a hierarchical organization of increasingly lineage-restricted progenitors, traditionally classified into the major branches of myelopoiesis (granulocyte development), erythropoiesis (red blood cell formation), megakaryocytopoiesis (platelet production), lymphopoiesis (lymphocyte development), and monocytopoiesis (monocyte formation). These progenitor cells, often referred to as “blasts” in their immature state, are morphologically indistinct within the bone marrow tissue. As a result, their identification and classification rely heavily on the use of cytogenetic, immunophenotypic, and molecular markers (9). A fundamental tool for characterizing hematopoietic cells is the expression of Cluster of Differentiation (CD) molecules, i.e., surface proteins that serve as hallmarks of cellular identity and developmental stage. CD markers are differentially expressed across hematopoietic lineages, thus enabling detailed tracking of differentiation trajectories. For instance, CD34 is typically expressed on early stem and progenitor cells, whereas CD117 (c-Kit), CD13, and CD33 are commonly associated with early myeloid progenitors. As monocytic differentiation progresses (Figure 1), CD33 marks early monoblasts (10), CD14 becomes detectable on promonocytes and mature monocytes (11), and CD11b is expressed on terminally differentiated monocytes and tissue-resident macrophages (12,13).

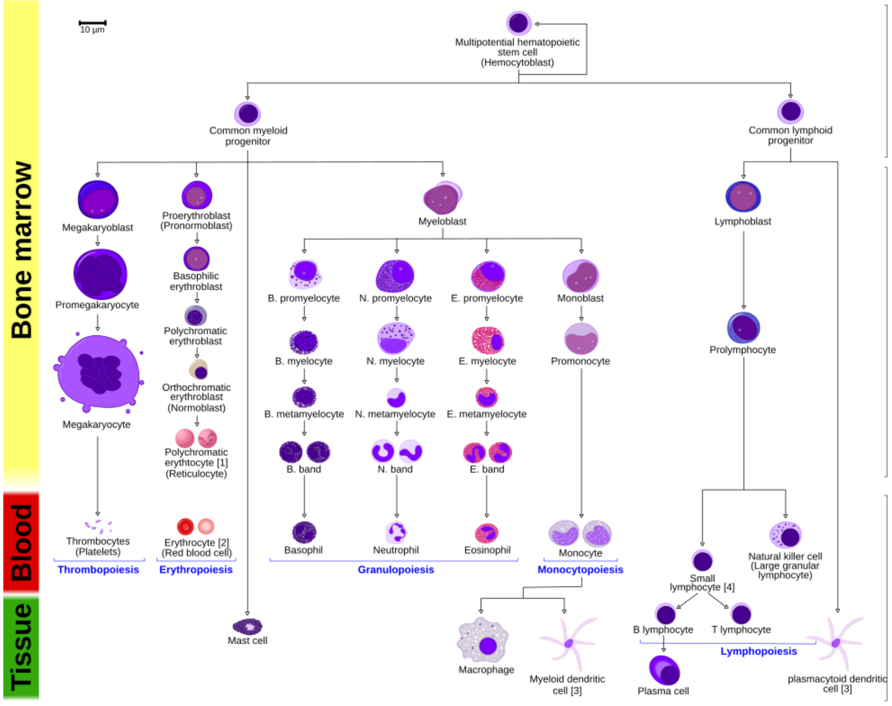

Figure 1. Schematic representation of human hematopoiesis [https://commons.wikimedia.org/wiki/File:Hematopoiesis_(human)_diagram.png]

1.2. Myelodysplastic Neoplasms (MDS) and Acute Myeloid Leukemia (AML)

Myelodysplastic Neoplasms (MDS) are a heterogeneous group of clonal myeloid disorders originating from HSCs dysfunction. They are characterized by ineffective hematopoiesis, peripheral cytopenias, morphological dysplasia, and a variable risk of progression to Acute Myeloid Leukemia (AML) (14,15). Diagnosis relies on persistent cytopenia, dysplasia in one or more myeloid lineages, and evaluation of bone marrow blasts. The 2022 World Health Organization (WHO) classification incorporates somatic mutation data, introducing entities such as MDS with *SF3B1* mutation or with biallelic TP53 inactivation, and emphasizes the role of clonal hematopoiesis in defining disease (14,15). Prognostic scoring systems, including IPSS, IPSS-R, and the molecularly integrated IPSS-M, combine clinical, cytogenetic, and mutational information to stratify patients by risk of AML progression and overall survival (16–18).

AML is a biologically and clinically heterogeneous malignancy, defined by the clonal expansion of poorly differentiated hematopoietic cells that impair normal myeloid differentiation. It can arise de novo or evolve from pre-existing MDS, in which case it is referred to as secondary or MDS-related AML, often associated with distinct molecular features and poorer prognosis (19–21). Although MDS and AML are distinct entities, they are intimately linked, and progression from MDS to AML generally reflects stepwise clonal evolution driven by the accumulation of additional genetic and epigenetic alterations (21).

1.2.1. Key Genetic and Epigenetic Alterations in MDS and AML

The advent of next-generation sequencing has enabled the identification of a broad spectrum of recurrent genetic alterations in MDS and AML, many of which converge on fundamental biological processes, such as RNA splicing, epigenetic remodeling and transcriptional regulation (22–25). *SF3B1*, *SRSF2*, *U2AF1*, and *ZRSR2* are among the most frequently mutated splicing factors. These mutations often represent early initiating events in MDS and contribute to the widespread disruption of pre-mRNA splicing and blockade of differentiation. They are typically heterozygous and mutually exclusive, and each lead to specific splicing alterations that result in reduced production of canonical transcripts and, consequently, a decrease in functional protein output (26–29). While splicing factor mutations are the most frequent in MDS, genes involved in epigenetic regulation, including TET2, DNMT3A, IDH1/2, ASXL1, and EZH2, are also commonly affected (30) (Figure 2). The sequential acquisition of such mutations, often in distinct combinations, underlies the evolution from indolent clonal hematopoiesis (CHIP) to overt disease and ultimately to leukemic transformation (30). Increasing attention has been directed towards understanding how these genetic alterations induce functional epigenetic dysregulation in myeloid malignancies. These mutations may disrupt normal patterns of DNA methylation and histone modifications, thereby reshaping the chromatin landscape and altering gene expression programs critical for hematopoietic differentiation and lineage commitment (Figure 2) (31). Mutations in *TET2* and *IDH1/2* lead to a reduction in 5-hydroxymethylcytosine (5hmC) and accumulation of 5-methylcytosine (5mC), resulting in transcriptional repression of genes essential for normal hematopoiesis (32,33). Importantly, a core methylation signature that is consistently present in both MDS and AML, independent of the specific genetic background, has been identified (33), suggesting that epigenetic disruption is not merely a consequence but a central driver of disease initiation and progression. Furthermore, the loss of proper epigenetic regulation enhances the clonogenic potential of mutated hematopoietic stem and progenitor cells and promotes resistance to therapy, particularly to DNA methyltransferase inhibitors (33).

TP53 mutations, more common in therapy-related cases and in patients with complex karyotypes, are linked to disease progression and therapy resistance in both MDS and AML (34). Furthermore, a study involving 44 high-risk MDS patients treated with azacitidine and lenalidomide identified the emergence of specific mutations in Phosphoinositide 3-kinases

(*PI3K)*, AKT serine/threonine kinase 3 (*AKT3)*, and Phospholipase C γ2 *(PLCG2)* during therapy. These mutations, located in key functional domains of the encoded proteins, were associated with reduced treatment response and shorter overall survival. Their presence may therefore promote aberrant cellular proliferation and disruption of normal myeloid differentiation, thereby facilitating drug resistance and disease progression towards acute leukemia (35).

Although MDS share several genetic alterations with AML, this latter also harbors mutations more specific to leukemic transformation, including activating mutations in signaling genes (*FLT3*, *NRAS*, *KRAS*, *KIT*) and transcription factors (*RUNX1*, *CEBPA*, *GATA2*). For instance, *FLT3*-ITD is found in up to 30% of AML cases but is rare in MDS, whereas biallelic *CEBPA* mutations define a favorable AML subset (36).

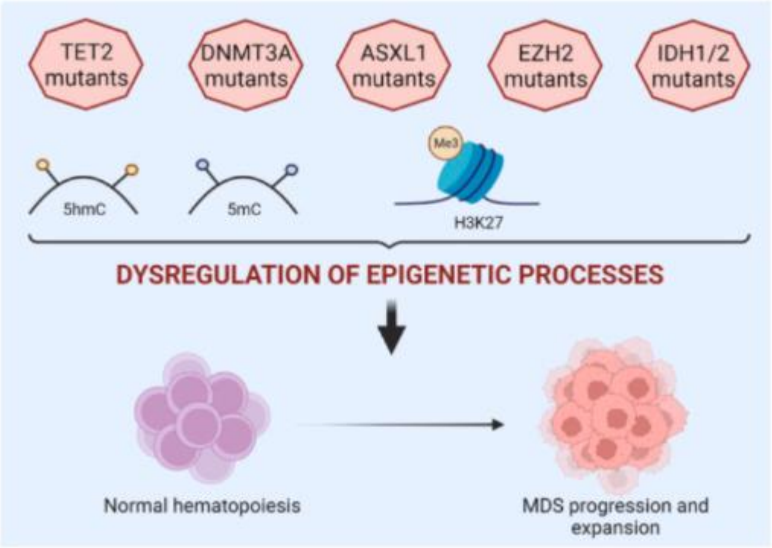

Figure 2. Key epigenetic alterations in MDS/AML (37)

1.2.1.1. Epigenetic alterations of PDZD2 in MDS/AML

Locus-specific and genome-wide methylation analyses have consistently demonstrated that PDZ domain-containing protein 2 (*PDZD2*) gene is frequently silenced via promoter hypermethylation in myeloid malignancies. Epigenomic profiling conducted by Dr. Figueroa and colleagues revealed pervasive and biologically relevant DNA methylation alterations in AML and MDS, with *PDZD2* emerging as a gene recurrently hypermethylated in leukemic samples. Independent datasets corroborated these findings, showing that *PDZD2* is silenced in approximately 90% of AML cases, consistent with epigenetic repression as a common mechanism of gene inactivation (38). In normal hematopoiesis, *PDZD2* is expressed in hematopoietic stem and progenitor cells and erythroid progenitors, but its expression is almost universally lost in AML, highlighting its potential role as a tumor suppressor within an epigenetically deregulated pathway contributing to leukemic transformation (39). PDZD2 exhibits a multidomain architecture (Figure 3), characterized by the presence of four PDZ motifs distributed along its primary sequence, which confer protein–protein and protein–lipid interaction capabilities, essential for the assembly of signaling complexes and the regulation of cellular polarity, receptor clustering, and signal transduction (40–43). PDZ motifs are highly conserved modules of approximately 90 amino acids, containing a canonical binding groove that typically recognizes C-terminal sequences of target proteins but can also interact with internal peptide motifs and membrane lipids, thereby contributing to functional versatility (41,44,45). PDZD2 also harbors caspase-sensitive motifs that mediate proteolytic cleavage, generating a secreted ~37 kDa fragment (sPDZD2) encompassing two PDZ domains. This cleavage is blocked by caspase inhibitors, and mutation of the caspase recognition sites prevents secretion, as demonstrated by immunoblotting studies (46). Additionally, PDZD2 contains a functional Nuclear Localization Signal (NLS) that regulates nuclear import. Mutations of basic residues within the NLS results in redistribution of the protein from the nucleus to the cytoplasm, suggesting a dual mode of action encompassing both nuclear and extracellular functions (46). Collectively, these structural features enable PDZD2 to function as a scaffold for receptor and channel positioning, modulation of cellular polarity, and regulation of signaling pathways critical for cell proliferation and differentiation, with direct implications for tumor suppressive activity (40,41,47,48).

Beyond hematopoiesis, PDZD2 biology has been explored in several systems, including the generation of a secreted ~37 kDa fragment (sPDZD2) reported to exert tumor-suppressive effects in solid tumor models, as well as roles in pancreatic progenitor cell behavior and prostate cancer (46,49,50). Recent data presented by Dr. Marlise Guerrero and colleagues indicate that PDZD2 is critical for hematopoietic homeostasis and that the secreted sPDZD2 exerts tumor-suppressive activity in preclinical models of AML. Loss of PDZD2 impairs erythroid differentiation, whereas treatment with recombinant sPDZD2 inhibits leukemic cell proliferation and promotes differentiation (39,51).

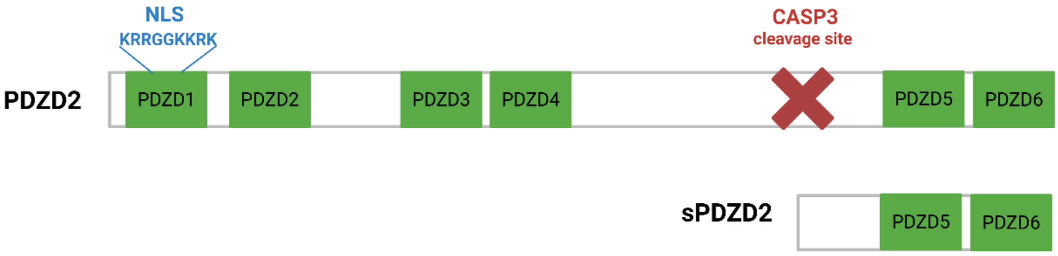

Figure 3. PDZD2 domain architecture [Created in https://BioRender.com]

1.2.2. MDS Pharmacological Treatment: Azacitidine (AZA) and Venetoclax (VEN)

In lower-risk MDS (LR-MDS), treatment aims to improve cytopenia and quality of life, using agents such as erythroid-stimulating agents, Lenalidomide (for del(5q)), Luspatercept (for ring sideroblasts), or immunosuppressive therapy in selected cases, whereas iron chelation may be considered in transfusion-dependent patients (17,52). In high-risk MDS (HR-MDS), hypomethylating agents (HMAs) are the standard of care, while allogeneic hematopoietic stem cell transplantation remains the only curative option for eligible patients. Upon HMA failure, therapeutic options are limited, and clinical trial enrollment is advised (17,22).

Azacitidine (AZA) is a synthetic nucleoside analogue structurally related to cytidine, distinguished by the substitution of the carbon atom at position 5 of the pyrimidine ring with nitrogen. This modification underlies its function as a DNA methyltransferase (DNMT) inhibitor. Following cellular uptake via nucleoside transporters, AZA is sequentially phosphorylated by uridine cytidine kinase to its mono-, di-, and triphosphate forms. The triphosphate derivative follows two major fates: approximately 80–90% is incorporated into RNA, where it interferes with RNA metabolism and protein synthesis, thereby inducing cytotoxic and pro-apoptotic effects. The remaining fraction is reduced by ribonucleotide reductase to generate the deoxyribonucleotide form, which becomes incorporated into DNA during replication (53,54) (Figure 4). DNA incorporation is particularly relevant for AZA epigenetic effects: covalent trapping of DNMT enzymes during DNA synthesis results in their degradation, leading to a global reduction in DNA methylation. This hypomethylating activity promotes re-expression of previously silenced genes, including tumor suppressors, and facilitates cellular differentiation. In parallel, incorporation into DNA may also trigger DNA damage responses, amplifying AZA cytotoxicity (55). Despite its clinical benefit, AZA may induce partial and transient responses, underscoring the need for more effective combinatorial strategies (56). That is why the combination of AZA and VEN, already used in AML, is gaining attention in HR-MDS (57).

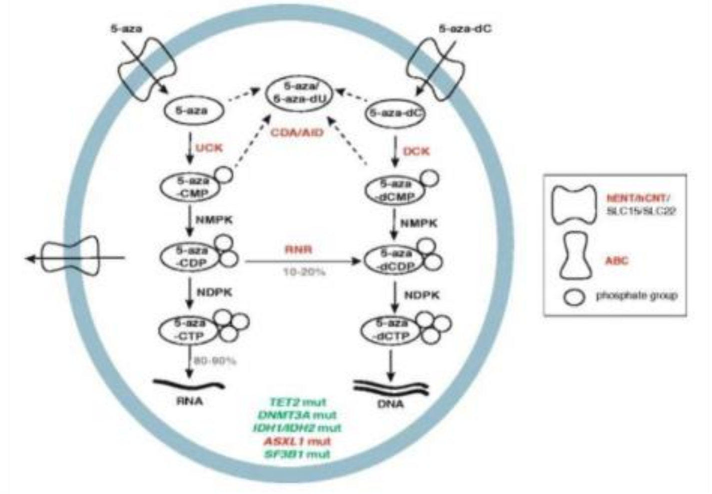

Figure 4. Mechanism of action of Azacitidine (58).

Venetoclax (VEN; ABT-199) is a highly selective, orally bioavailable small molecule designed to specifically target the BH3 domain of the anti-apoptotic protein B-cell lymphoma-2 (BCL2) (Figure 5). In many myeloid malignancies, *BCL2* is overexpressed and is associated with resistance to apoptosis and poor prognosis, allowing cancer cells to evade apoptosis by neutralizing BH3-only proteins, thereby promoting survival and proliferation (59,60). As a BH3 mimetic, VEN binds with high affinity to the BH3-binding pocket of BC-2, competitively displacing pro-apoptotic BH3-only proteins. Freed from sequestration, these BH3-only proteins can activate BCL2 associated X apoptosis regulator (BAX) and BCL2 antagonist/killer 1 (BAK1), facilitating mitochondrial permeabilization and apoptotic cell death. This mechanism effectively restores the apoptotic pathway in tumor cells reliant on BCL2-mediated survival signals (59,61,62). However, resistance to VEN can develop, frequently associated with the upregulation of alternative anti-apoptotic proteins, such as MCL1, which can compensate for BCL2 inhibition and maintain cellular viability (63,64).

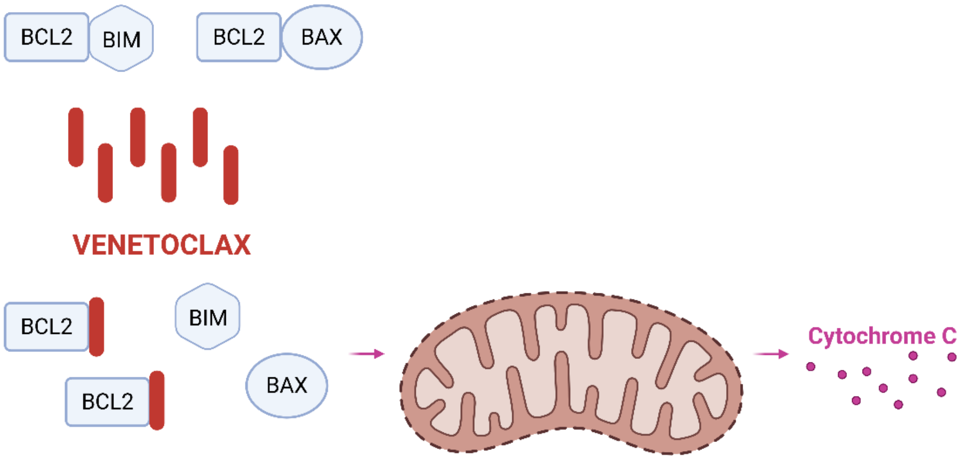

Figure 5. Mechanism of action of Venetoclax [Created in https://BioRender.com].

Early-phase clinical studies demonstrated encouraging response rates and survival benefits, supporting VEN potential incorporation into the therapeutic landscape of HR-MDS (56). Early-phase data from Zeidan et al. reported promising overall response rates (ORR) and a median overall survival (OS) of 12.6 months in relapsed/refractory HR-MDS after HMA failure, with a favorable safety profile for AZA and VEN (65). Similarly, Braish et al. reported an ORR of 49% and a median OS of 7 months in a phase I/II study, confirming the feasibility and tolerability of the combination, but also noting that the combination did not significantly improve clinical outcomes compared to historical controls (66). Even the VERONA trial (NCT04401748), that is assessing the efficacy and safety of AZA and VEN compared to AZA vs placebo in previously untreated patients with MDS with IPSS-R intermediate, high or very high (67), has not yet shown statistically significant improvement in OS. That is why secondary analyses are ongoing to identify subgroups that may benefit from this therapy and are trying to elucidate mechanisms of resistance (66).

AZA, through its hypomethylating activity, has been shown to downregulate MCL1, a key anti-apoptotic protein commonly implicated in resistance to BCL2 inhibition, and to upregulate the BH3-only protein NOXA, which further antagonizes MCL1 function. Moreover, AZA has been shown to interfere with mitochondrial metabolism, including oxidative phosphorylation, thereby impairing the bioenergetic capacity of leukemic stem cells and amplifying their susceptibility to apoptosis (68). These effects may sensitize leukemic cells also to VEN-induced apoptosis, by reducing the available pool of anti-apoptotic proteins and enhancing the activity of pro-apoptotic effectors like BAX and BAK1 (69,70). Additional studies confirm that the combination of AZA and VEN achieves a dual blockade of anti-apoptotic pathways, through direct inhibition of BCL2 and indirect suppression of MCL1 expression, while also modulating immune-related and oxidative stress pathways that may contribute to the anti-leukemic effect (61,71,72). However, despite the significant therapeutic potential of this strategy, acquired resistance remains a major clinical challenge. Emerging evidence suggests that resistance may be mediated by compensatory upregulation of alternative anti-apoptotic proteins, such as MCL1 and BCL-XL, thereby restoring mitochondrial integrity and promoting cell survival in the face of BCL2 inhibition (63,73). These findings underscore the need for continued investigation into the complex regulatory networks involved in AZA+VEN response and resistance, with the goal of identifying rational combination therapies that can overcome resistance and improve patient outcomes.

1.3. The Apoptotic Pathway

Apoptosis is a tightly regulated form of programmed cell death, crucial for maintaining tissue homeostasis and eliminating damaged or unwanted cells (Figure 6). The apoptotic process is primarily mediated through the activation of a family of cysteine-aspartic proteases known as Caspases. These enzymes exist as inactive zymogens and are activated by proteolytic cleavage in response to specific stimuli. Caspases are generally classified into initiator (such as Caspase-8 and Caspase-9), which begin the signaling cascade, and effector caspases (such as Caspase-3, -6, and -7), which execute the death program by cleaving various structural and regulatory proteins (74).

Two main processes can lead to caspase activation: the extrinsic (receptor-mediated) and the intrinsic (mitochondrial) pathways (Figure 6). Although both of them converge on the activation of executioner caspases, the intrinsic pathway is particularly relevant in the context of cellular stress and is tightly controlled by the BCL2 protein family (75,76). The intrinsic apoptotic pathway is activated by intracellular stress signals such as DNA damage, oxidative stress, cytotoxic drugs, or calcium overload. These stimuli lead to mitochondrial outer membrane permeabilization (MOMP), a critical and irreversible step in the apoptotic process. MOMP results in the release of pro-apoptotic factors, such as cytochrome c, into the cytosol, where they bind to Apaf-1 and pro-Caspase-9 to form the apoptosome. This complex promotes the autocatalytic activation of Caspase-9, which then cleaves and activates downstream effector caspases, especially Caspase-3 (77,78). The regulation of MOMP is orchestrated by the interplay between pro- and anti-apoptotic members of the BCL2 protein family (79). Anti-apoptotic proteins, such as BCL2 and MCL1, maintain mitochondrial integrity, while pro-apoptotic effectors like BAX and BAK1 oligomerize and form pores in the mitochondrial membrane, enabling the release of cytochrome c. BH3-only proteins, including BCL2-like 11(*BCL2L11*; BIM), p53 upregulated modulator of apoptosis (*BBC3*; PUMA), and BIK, further modulate this balance by either directly activating BAX/BAK1 or by neutralizing anti-apoptotic proteins (80,81). When cellular damage is sensed, BH3-only proteins are upregulated or activated, tipping the balance in favor of apoptosis. BIM and PUMA play critical roles in sensing genotoxic stress and in promoting the activation of BAX and BAK1, while simultaneously sequestering BCL2 and MCL1 to relieve their inhibitory effects. Once BAX and BAK1 are activated, the apoptotic cascade proceeds irreversibly (82). Caspase-3, the central executioner caspase, cleaves a wide range of cellular substrates, including the DNA repair enzyme poly(ADP-ribose) polymerase (PARP), whose inactivation further accelerates apoptotic progression by preventing DNA repair and enhancing chromatin fragmentation (83).

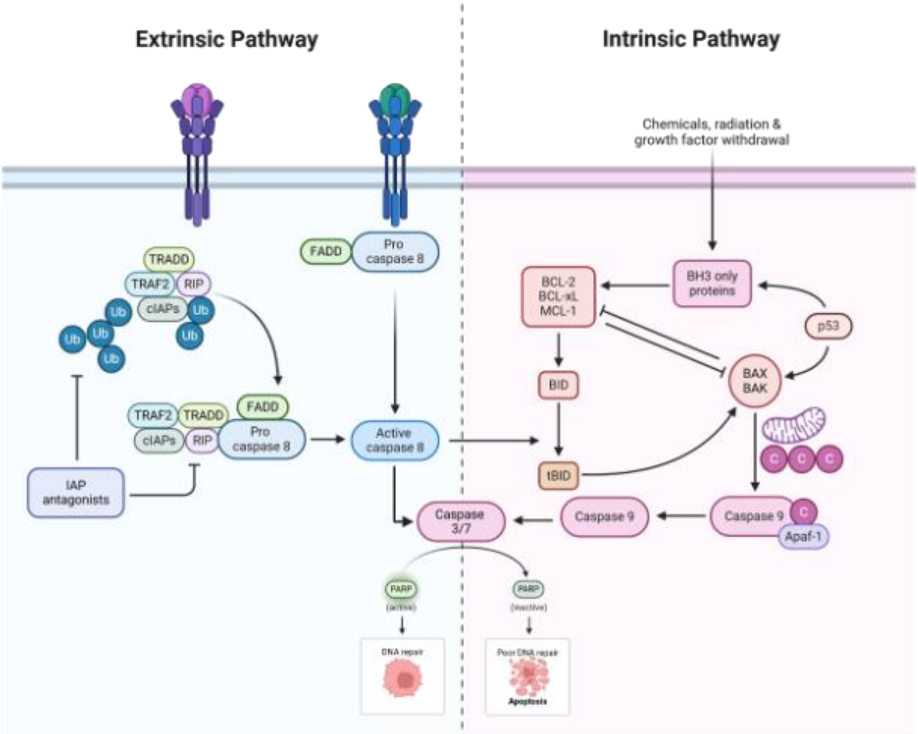

Figure 6. Apoptotic pathway [Created in https://BioRender.com].

In leukemia, the relative expression and activity of BH3-only proteins, BAX/BAK1, and anti-apoptotic BCL2 family members determine the sensitivity of leukemic cells to chemotherapeutic agents and BH3 mimetics (83,84). While caspase-independent mechanisms involving mitochondrial proteins such as AIF and Endonuclease G exist, the caspase-dependent pathway, especially the regulation by BCL2 family dynamics, remains the principal mechanism in most leukemic contexts (79,85).

1.4. Phosphoinositide-dependent Signaling

Phosphoinositides (PIs) are a family of phosphorylated derivatives of phosphatidylinositol, localized primarily to the cytoplasmic leaflet of eukaryotic cell membranes. From a structural point of view, they consist of a hydrophobic group bound to two fatty acid chains. Although they constitute a minor fraction of total cellular lipids, they play essential roles in regulating membrane identity, vesicular trafficking, cytoskeletal dynamics, and signal transduction (Figure 7) (86). There are seven naturally occurring PI species, each defined by the phosphorylation pattern on the inositol ring at the D3, D4, and D5 positions, and each enriched in specific subcellular compartments, thereby recruiting distinct sets of effector proteins to those membranes (87–89) (Figure 7). PIs are dynamically interconverted by specific lipid kinases and phosphatases, which are tightly regulated and compartmentalized (90,91). Dysregulation of PI metabolism is implicated in a range of human diseases, including cancer, metabolic disorders, neuropathies, and rare genetic syndromes. Mutations in phosphoinositide kinases or phosphatases can disrupt normal signaling and membrane trafficking, leading to pathophysiological consequences (92–94).

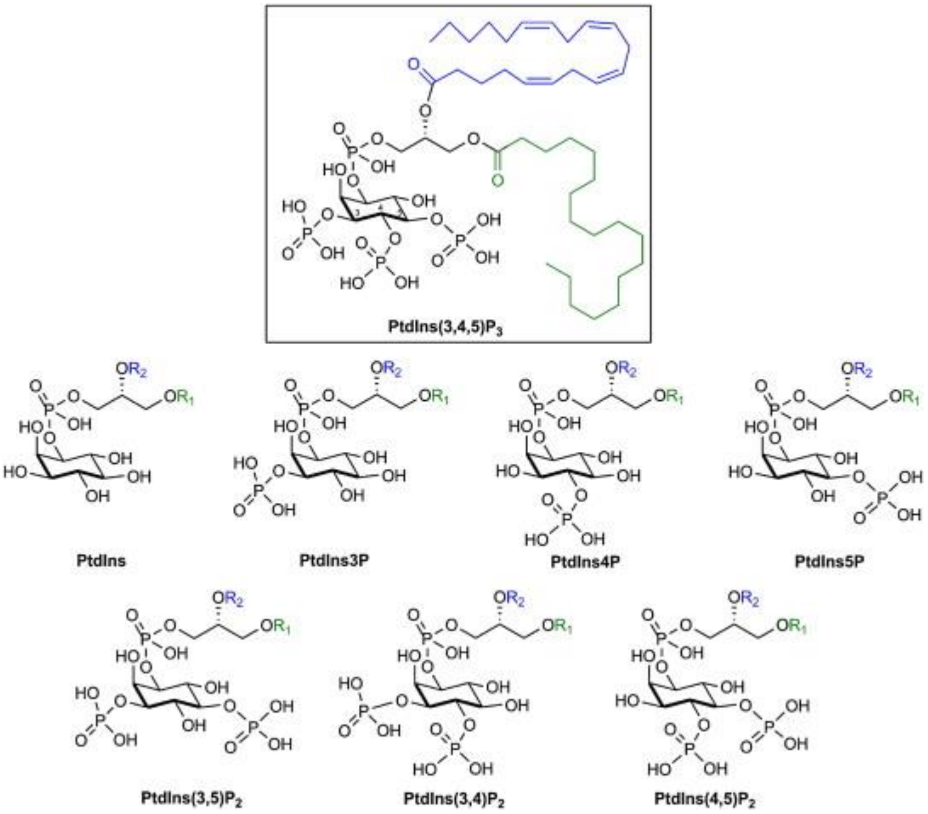

Figure 7. Structure of Phosphoinositides (95).

1.4.1. Phospholipase C (PLC)/Protein Kinase C (PKC) Axis

Phospholipases C (PLCs) enzymes constitute a critical family of signaling molecules involved in the transduction of extracellular stimuli into intracellular responses (Figure 8). In humans, at least six classes of PLCs (β, γ, δ, ε, ζ, and η) have been identified, further divided into 13 classical and 3 atypical isoforms, each with specific structural features, activation mechanisms, and tissue distribution. PLCs share catalytic X and Y domains but have distinct accessory domains that determine their regulation and subcellular localization (96–98). PLC activation can occur through interaction with heterotrimeric G proteins (particularly Gαq and Gβγ subunits for PLCβ), receptor and non-receptor tyrosine kinases (PLCγ), small GTPases (PLCε, and some PLCβ and PLCγ), and calcium (PLCδ) (96,98–100). Some PLC isoforms, such as PLCε, also have additional regulatory functions, including guanine nucleotide exchange factor (GEF) or GTPase-activating protein (GAP) activity, in addition to their lipase function (101).

There is strong evidence that PLC isoforms, particularly the PLCβ and PLCγ subfamilies, play central roles in the regulation of hematopoiesis and malignant transformation (102). PLCβ (PLCβ1–β4) isoforms are activated by G protein-coupled receptors and localize to the cytoplasm and nucleus, where they regulate essential intracellular signaling pathways (91). PLCβ1, encoded on chromosome 20p12 (103), has two splicing variants, PLCβ1a (150 kDa) and PLCβ1b (140 kDa), that differ in their C-terminal domain and subcellular distribution, with PLCβ1a present in both cytoplasm and nucleus and PLCβ1b mainly nuclear (104,105). In hematopoietic stem and progenitor cells (HSPCs), PLCβ1 regulates cell cycle progression via cyclin D3, influencing G1/S and G2/M transitions (106–108). It also contributes to lineage differentiation, with high expression during myeloid and low during erythroid programs, indicating a lineage-specific role (109). Monoallelic deletion of *PLCB1* occurs in ~44% of MDS cases, ~66% of which progress to AML, correlating with reduced expression and serving as an independent prognostic marker (110,111). At the epigenetic level, *PLCB1* promoter hypermethylation is common in HR-MDS, while AZA-induced demethylation restores expression. Increased *PLCB1* during treatment is associated with myeloid differentiation and durable clinical responses, supporting its role as a direct molecular target of AZA in MDS and AML (112–115).

The PLCγ subfamily comprises two isoforms, PLCγ1 and PLCγ2, which are primarily activated by receptor tyrosine kinases but can also be directly stimulated by lipid-derived second messengers in the absence of tyrosine phosphorylation (116). Despite structural and regulatory similarities, the two isoforms fulfill distinct, non-redundant functions, as loss of one cannot be compensated by the other (117).

PLCγ1 is encoded on chromosome 20q and is ubiquitously expressed, where it regulates essential cellular processes including proliferation, migration, and apoptosis. Its activity is tightly controlled by PI3K signaling (86). In hematopoiesis, PLCγ1 contributes to both erythroid and myeloid differentiation, with expression levels increasing during erythroid commitment and decreasing during myeloid lineage specification, suggesting a lineage-specific role (107).

PLCγ2, in contrast, is selectively expressed in HSPCs and is indispensable for myeloid differentiation, mirroring the behavior of PLCβ1 (118). Dysregulation or mutation of *PLCG2* has been implicated in the pathogenesis of hematologic malignancies, including leukemias and lymphomas (118). Of clinical relevance, specific point mutations in *PLCG2* have been associated with therapy resistance in HR- MDS, especially during disease progression and in response to hypomethylating agents such as AZA (35).

PLCG2 expression is strongly induced by cytokines, such as M-CSF and G-CSF, and it is involved in immune cell maturation. Mechanistically, cytokine signaling activates PLCγ2-dependent hydrolysis of phosphatidylinositol 4,5-bisphosphate (PIP2), producing inositol 1,4,5-trisphosphate (IP3) and diacylglycerol (DAG). IP3 facilitates the mobilization of calcium ions from intracellular stores, while DAG remains embedded in the plasma membrane (119), where it acts as a key activator of PKC, a family of serine/threonine kinases involved in the regulation of numerous cellular processes, including proliferation, differentiation, motility, survival, secretion, and exocytosis (120), and promoting myeloid lineage commitment (121,122) (Figure 8). Once activated, PKC phosphorylates a variety of cytoplasmic and nuclear substrates, influencing cell cycle progression, cytoskeletal dynamics, and transcriptional programs (120,123,124). Among its downstream effects, PKC can activate the MAPK/ERK signaling cascade (120), promote vesicle fusion in secretory cells, such as neurons and pancreatic β-cells, and modulate synaptic plasticity and memory formation in the nervous system (123–125). Additionally, PKC plays a context-dependent role in apoptosis, exerting either pro- or anti-apoptotic effects depending on the specific isoform and cellular environment (120,123). There are several isoforms of PKC, the most common of which are PKCα, PKCβ, and PKCγ (126,127). Among the PKC isoforms implicated in myeloid malignancies, PKCα has emerged as a critical modulator of leukemic cell behavior. PKCα promotes cell survival and proliferation, particularly in FLT3-ITD–mutated AML, where PKCα activity sustains leukemic cell viability and contributes to disease aggressiveness.

Inhibition of PKCα then results in reduced proliferation and the induction of apoptosis, highlighting its potential as a therapeutic target in genetically defined AML subsets (128). In MDS, PKCα plays a distinct role in promoting erythroid differentiation and modulating cell cycle dynamics. Notably, in patients with del(5q), nuclear translocation of PKCα has been associated with the erythroid maturation effects of lenalidomide treatment. This nuclear localization is thought to contribute to cell cycle arrest and lineage-specific differentiation, suggesting that PKCα may act as a mediator of therapeutic response in MDS (129,130).

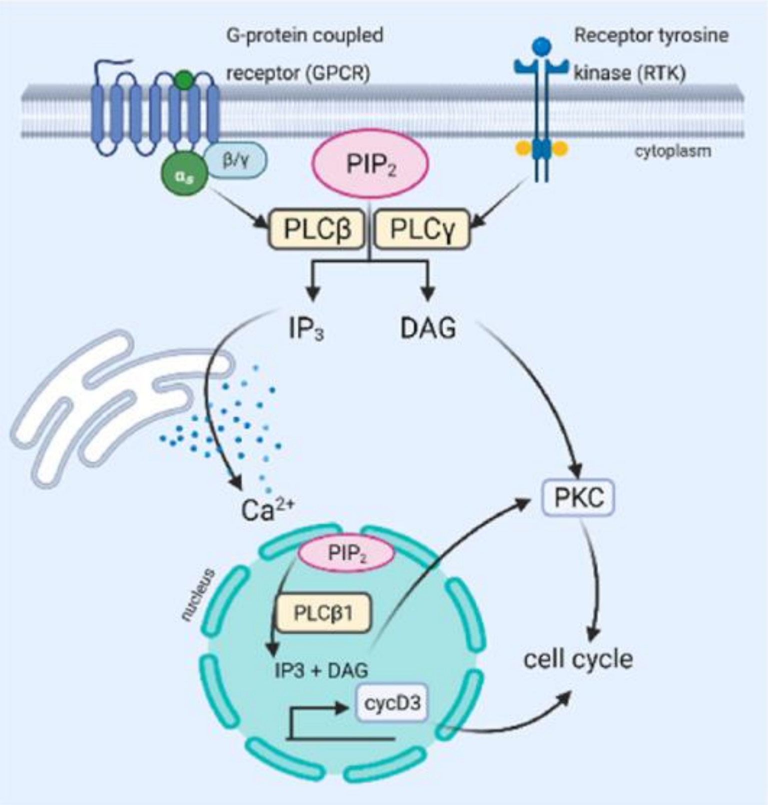

Figure 8. PLC / PKC axis (37).

1.4.2. AKT / Glycogen Synthase Kinase 3 (GSK3) Axis

One of the most critical PI-dependent signaling cascades involved in cellular homeostasis and transformation is the PI3K/AKT/ Glycogen Synthase Kinase 3 (GSK3) axis (Figure 9). This pathway regulates a broad spectrum of biological processes including cell proliferation, metabolism, differentiation, survival, and angiogenesis, and is frequently dysregulated in malignancies, including myeloid neoplasms (131). The pathway is typically activated upon engagement of receptor tyrosine kinases (RTKs) or G protein-coupled receptors (GPCRs) by extracellular ligands, leading to the recruitment of PI3Ks to the plasma membrane. Class I

PI3Ks, composed of a regulatory and a catalytic subunit, catalyze the phosphorylation of PIP2 to generate phosphatidylinositol-3,4,5-trisphosphate (PIP3), a key lipid second messenger. PIP3 accumulation is tightly regulated by the tumor suppressor Phosphatase and tensin homolog (PTEN), which acts as a lipid phosphatase to reverse this reaction (132). The generation of PIP3 facilitates the membrane recruitment of pleckstrin homology (PH)-domain-containing proteins such as 3-phosphoinositide-dependent protein kinase 1 (PDK1) and AKT. Subsequent phosphorylation of AKT at key threonine and serine residues by PDK1 and mechanistic target of rapamycin complex 2 (mTORC2), respectively, leads to its full activation and translocation to the cytoplasm and nucleus, where it phosphorylates a variety of substrates that control cell cycle progression and apoptosis (133–135).

Among the downstream effectors of AKT, GSK3 plays a central role. GSK3 is a ubiquitously expressed serine/threonine kinase existing in two isoforms, GSK3α and GSK3β, encoded by distinct genes (*GSK3A* on chromosome 19 and *GSK3B* on chromosome 3). Both isoforms are negatively regulated by AKT through phosphorylation at Ser21 (GSK3α) and Ser9 (GSK3β), which inhibits their kinase activity (136). Inactivation of GSK3 downstream of AKT promotes survival signaling by impairing the phosphorylation and degradation of anti-apoptotic proteins, such as MCL1, and by preventing activation of pro-apoptotic factors like BAD (137). GSK3 integrates signals not only from the PI3K/AKT axis but also from pathways such as Wnt/β-catenin and PLC/PKC (138), contributing to the fine-tuned regulation of metabolism, transcriptional control, RNA processing, and microRNA biogenesis (Figure 10) (139,140).

In the context of MDS, the PI3K/AKT pathway is differentially activated depending on disease severity: low-risk patients exhibit only modest phosphorylation of AKT, whereas HR-MDS and AML cases display marked activation of this axis, which is absent in normal hematopoietic progenitors (132). This constitutive activation contributes to leukemic transformation and disease progression by enhancing pro-survival signaling and resistance to apoptosis. GSK3, particularly the β isoform, is a key player in hematopoietic stem and progenitor cell regulation (141,142), and its aberrant activity has been implicated in the pathogenesis of both MDS and AML (143,144). Notably, GSK3β activity has been shown to support leukemic stem cell maintenance and promote therapeutic resistance (145–147). In AML, AKT-mediated inhibition of GSK3β fosters the stabilization of BCL2 family proteins, thereby impairing apoptotic responses and enhancing cell survival even in the face of chemotherapy (148,149).

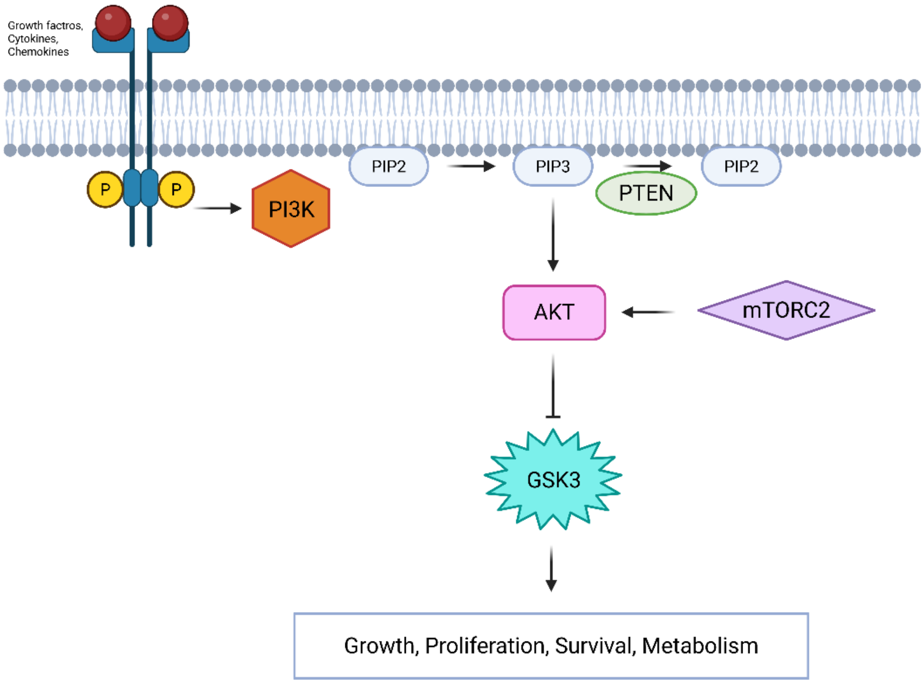

Figure 9. AKT/GSK3 axis [Created in https://BioRender.com].

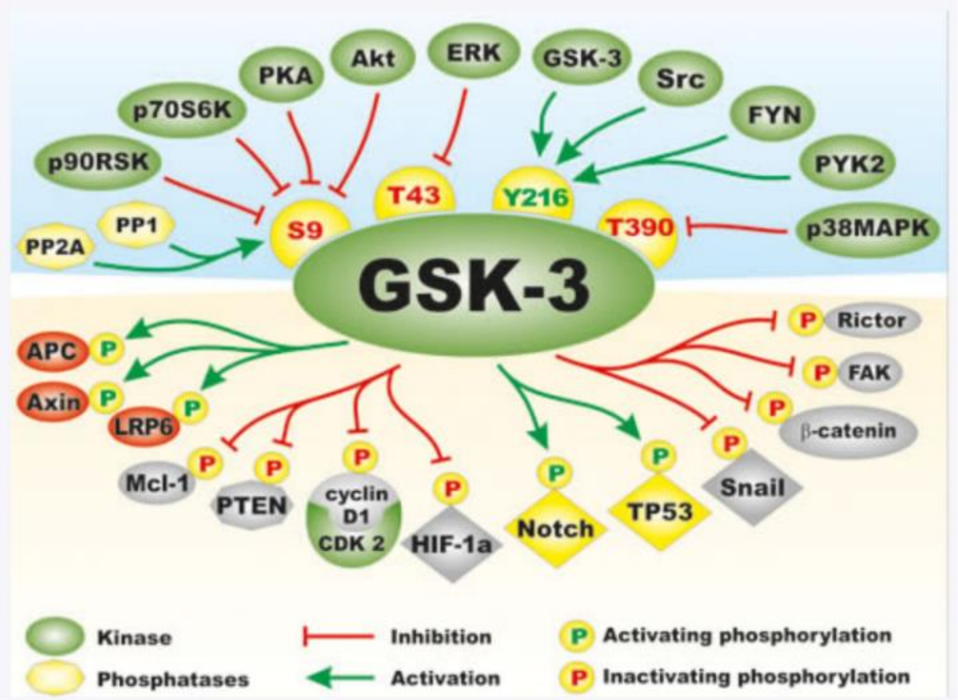

Figure 10. Regulation of GSK3 activity and GSK3 downstream targets (150).

2. AIM OF THE STUDY

MDS and AML are hematologic malignancies characterized by ineffective hematopoiesis, impaired differentiation of HSCs, and profound epigenetic dysregulation. These alterations underlie disease heterogeneity and contribute to therapy resistance and leukemic progression, highlighting the need for mechanistic insights that can guide therapeutic innovation.

Within this framework, the present study was designed with two complementary aims. First, we aimed to investigate the molecular mechanisms of AZA and VEN, administered alone or in combination. We focused specifically on two pathways already implicated in MDS pathogenesis and AML progression: the PI signaling cascade, involving PLC/PKC and AKT/GSK3 axis, and the apoptotic pathway. To this end, we employed both *ex vivo* analyses of MDS patient-derived cells and leukemic cell lines, with the goal of clarifying how AZA+VEN impacts survival, differentiation, and apoptotic regulation.

Second, we sought to establish a CRISPR-Cas9–based genome editing strategy to study the role of PDZD2, a poorly characterized factor that is found hypermethylated in nearly 90% of AML cases. Given its strong epigenetic regulation, PDZD2 represents a compelling candidate regulator of hematopoiesis. Through the development and optimization of genome-editing approaches, this work sets the stage for future studies aimed at delineating the contribution of PDZD2 to normal and malignant hematopoietic differentiation.

Overall, this dual approach integrates a translational dimension, centered on deciphering the action of AZA+VEN in HR-MDS, with a mechanistic perspective focused also on PDZD2, thereby unifying both projects under the overarching theme of epigenetic regulation in myeloid malignancies.

3. MATERIALS AND METHODS

3.1. *Ex vivo* Analyses

3.1.1. High-risk MDS Patients

This study involved the analysis of peripheral blood (PB) samples obtained from eight patients newly diagnosed with HR-MDS (7/8 R-IPSS high or very-high, 1/8 R-IPSS intermediate-risk), according to the Revised International Prognostic Scoring System (R-IPSS). All patients were enrolled at the Institute of Hematology "L. e A. Seràgnoli," IRCCS—Azienda Ospedaliero-Universitaria di Bologna, University of Bologna, in accordance with the principles of the Declaration of Helsinki. Clinical responses and overall outcomes were evaluated based on the revised criteria of the International Working Group (IWG).

Patients received AZA at a dose of 75 mg/m² per day for seven consecutive days in a 28-day cycle, either as monotherapy or in combination with VEN (400 mg orally, once daily on days 1–14). Only those who completed at least two full treatment cycles and underwent formal disease assessment were included in the molecular analysis.

3.1.2. Isolation of Mononuclear Cells

For *ex vivo* analyses, mononuclear cells (MNCs) were isolated from patient samples using density gradient centrifugation with Ficoll-Paque (Amersham Biosciences, Uppsala, Sweden), following the manufacturer's instructions. Samples were collected at baseline (T0, prior to treatment initiation) and at defined time points during therapy, specifically after 2, 4, 6, 10 and 14 cycles of therapy (T2, T4, T6, T10, and T14).

3.1.3. Genomic DNA extraction and *BCL2* Mutational Analysis

To assess mutational status at baseline, genomic DNA was extracted from MNCs collected at T0 using the QIAamp DNA Blood Mini Kit (Qiagen Ltd), following standard protocols. DNA concentration was determined with the Qubit™ 1X dsDNA High Sensitivity (HS) Assay Kit (Thermo Fisher Scientific). *BCL2* mutational status was assessed using a next-generation capture-based target panel (Lymphoma Solution; SOPHiA GENETICS, Saint Sulpice, Switzerland), and the output data were analyzed using SOPHiA DDM™ (SOPHiA Genetics) as previously described for blood samples (151). *BCL2* variants with coverage greater than 2000× and variant allele frequency (VAF) >2% were retained.

3.2. Cell Culture

Due to the lack of *in vitro* MDS experimental models, this study employed AML-derived cell lines to investigate the molecular mechanisms of interest. Specifically, the THP-1 and MV4-11 cell lines were used, alongside HEK293 cells for genome editing experiments.

THP-1 cells are a human monocytic leukemia cell line originally isolated from the peripheral blood of a patient with acute monocytic leukemia (Figure 11). THP-1 cells were cultured at 37°C in a humidified atmosphere containing 5% CO_2, using RPMI-1640 medium supplemented with 10% fetal bovine serum (FBS) and 1% L-glutamine (Corning). Cells were seeded at an initial density of 3×10^5 cells/mL and subsequently split three times per week when reaching a density of approximately 8×10^5 cells/mL.

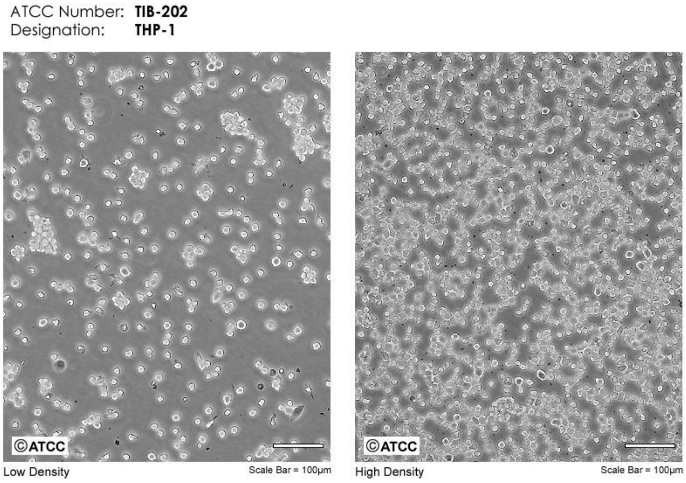

Figure 11. THP-1 cells (ATCC – American Type Culture Collection)

MV4-11 is a human AML cell line harboring the FLT3-ITD mutation, commonly used as a model for HR-AML (Figure 12). MV4-11 cells were maintained under culture conditions similar to THP-1 cells, using RPMI-1640 medium supplemented with 10% FBS and 1% L-glutamine (Corning) at 37°C in a 5% CO_2 atmosphere.

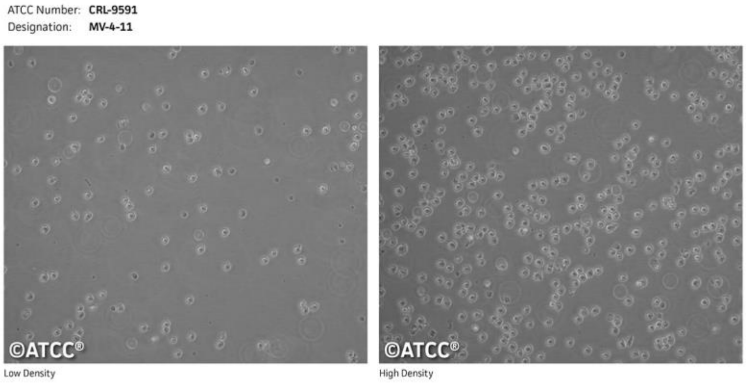

Figure 12. MV4-11 cells (ATCC – American Type Culture Collection)

HEK293 cells are human embryonic kidney cells widely used for genetic manipulation due to their high transfection efficiency (Figure 13). HEK293 cells were cultured in Dulbecco's Modified Eagle Medium (DMEM, #11965092, Gibco$^{\text{TM}}$) supplemented with 10% FBS and 1% L-glutamine (Corning), maintained at 37°C with 5% CO_2 in a humidified incubator.

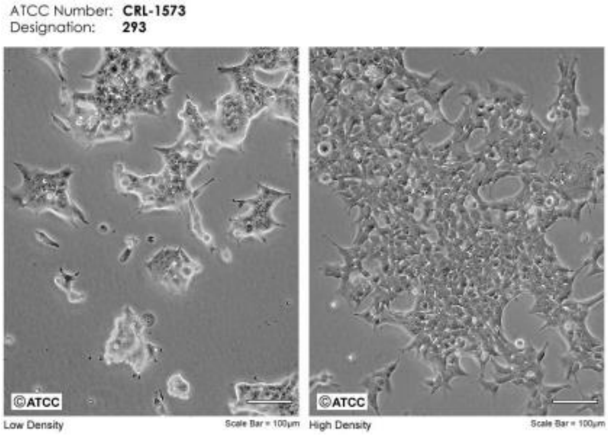

Figure 13. HEK293 cells (ATCC – American Type Culture Collection)

3.3. Pharmacological Treatment

In this study, initial experimental procedures included four treatment conditions for each cell line: untreated control, single-agent AZA (HY-10586, MedChemExpress; stock: 100 mg/mL in DMSO), single-agent VEN (HY-15531, MedChemExpress; stock: 1mM in DMSO), and the combination of AZA and VEN. THP-1 cells were seeded at a density of 3×10^5 cells/mL and exposed to 5 µM AZA and 125 nM VEN, either individually or in combination. MV4-11 cells were seeded under identical conditions and treated with 5 µM AZA and 5 nM VEN. All treatments were administered at the time of seeding (T0), and cells were cultured for 24 hours under standard conditions without media replacement. At the end of the incubation period, cells were collected and processed for molecular and functional analyses.

3.4. Cytofluorimetric analyses

Throughout the study, flow cytometric evaluations were performed on both treated and control samples to assess cellular parameters. Analyses were conducted using the Attune NxT Acoustic Focusing Cytometer (Thermo Fisher Scientific).

3.4.1. Cell cycle analysis

Flow cytometric analysis was employed to quantify DNA content at the single-cell level, enabling the discrimination of cells across different phases of the cell cycle through propidium iodide (PI) staining. For each sample, 500 µL of cell suspension were collected after 24 hours of treatment, subsequently fixed with 1 mL of cold 70% ethanol (4°C) and stored overnight at -20°C. On the following day, cells were washed twice with PBS 1X and incubated with PI solution at a final concentration of 5 µg/mL (BMS500FI-300, eBioscience) in the dark for 30 minutes prior to flow cytometric acquisition through Attune NxT Acoustic Focusing Cytometer (Thermo Fisher Scientific).

3.4.2. Cell death analysis: AnnexinV/PI staining

Cell death was assessed by flow cytometry using Dead Cell Apoptosis Kits with Annexin V for Flow Cytometry (Invitrogen, V13245) following the manufacturer’s instructions. For each sample, 2×10^5 cells were collected and samples were analyzed promptly by Attune NxT Acoustic Focusing Cytometer (Thermo Fisher Scientific), using at least three independent biological replicates.

3.5. Gene expression analyses

3.5.1. RNA extraction

After 24 hours of treatment, samples containing 2×10^6 cells were collected from each experimental group to extract total RNA. RNA isolation was carried out using the Qiagen RNeasy Mini Kit (Qiagen), following the manufacturer’s instructions. The concentration and purity of the extracted RNA were then measured by spectrophotometry using a Nanodrop instrument (CELBIO S.p.A.).

3.5.2. Retrotranscription

Based on the quantification data obtained using the NanoDrop spectrophotometer, 1000 ng of total RNA were reverse-transcribed in a final volume of 20 μL using the High-Capacity cDNA Reverse Transcription Kit (ThermoFisher Scientific), following the manufacturer's protocol. Reverse transcription reactions were performed on a 2720 Thermal Cycler (ThermoFisher Scientific) under the following thermal conditions (Table 1):

Table 1. Retrotranscription reaction conditions

	1st Step	**2nd Step**	**3rd Step**	**4th Step**
Temperature (°C)	25	37	85	4
Time (min)	10	120	5	∞

3.5.3. Real-Time PCR with TaqMan probes

Real-Time PCR reactions were carried out using 96-well plates, each well containing 10 ng of cDNA in a final volume of 20 μL. The reaction mix included 10 μL of TaqMan Universal PCR Master Mix (Applied Biosystems), 1 μL of the appropriate TaqMan Gene Expression Assay (ThermoFisher Scientific), and RNase-free water. All samples were run in technical triplicates. Amplification was performed using the QuantStudio 1 Real-Time PCR System (ThermoFisher Scientific), and data were analyzed using the associated software. Gene expression was analyzed using the comparative Ct method ($2^{-\Delta\Delta Ct}$). For each sample, Ct values were first normalized to the endogenous control GAPDH (ΔCt), then compared to the untreated control sample to obtain ΔΔCt values. Relative quantification (RQ) was calculated as $2^{-\Delta\Delta Ct}$. The list of TaqMan probes used is provided in Table 2.

Table 2. qPCR TaqMan probes

Genes	**ID code**
PLCB1	Hs01001930_m1
PLCG1	Hs00234046_m1
PLCG2	Hs01101857_m1
CD33	Hs01076282_g1
ITGAM (CD11b)	Hs00167304_m1
CD14	Hs02621496_s1
BCL2	Hs00608023_m1
BCL2L11 (BIM)	Hs00708019_s1
BAX	Hs00180269_m1
BBC3 (PUMA)	Hs00248075_m1
BAK1	Hs00832876_g1
GAPDH	Hs02786624_g1

3.6. Protein extraction and Western Blot analyses

3.6.1. Protein extraction

To obtain protein lysates, cell lysis was performed using Mammalian Protein Extraction Reagent M-PER lysis buffer (Thermo Fisher Scientific, #78501) supplemented with Halt™ Protease and Phosphatase Inhibitor Cocktail (100X) (Thermo Fisher Scientific, #78440). Lysates were sonicated for 15 s at 70% power using a BANDELIN SONOPLUS sonicator (BANDELIN Electronic GmbH & Co. KG, Germany). Protein concentration was measured using Pierce™ Coomassie Plus (Bradford) Assay Reagent (Thermo Fisher Scientific).

3.6.2. Western Blot

For SDS-PAGE separation, a total of 30 µg of protein lysate was separated by SDS-PAGE using homemade 8% or 12% polyacrylamide gels, subsequently transferred onto nitrocellulose membranes for 1 hour at 4 °C using a constant power of 350 mA. Transfer efficiency and total protein distribution were assessed by staining the membranes with Ponceau S solution (Thermo Fisher Scientific) for 3 minutes. Membranes were then washed twice with 1X PBS/0.1% Tween-20 (PBST) to remove excess stain and blocked for 1 hour at room temperature under gentle agitation with a blocking buffer consisting of 5% non-fat dry milk in 1X PBST. Primary antibody incubation was carried out overnight at 4°C with antibodies diluted in either bovine serum albumin (BSA, Sigma-Aldrich) or milk according to the manufacturer's recommendations. A full list of primary antibodies used in this study is provided in Table 3. Membranes were then subjected to three additional PBST washes for 10 min before incubation with HRP-conjugated secondary antibodies (Thermo Fisher Scientific) for 1 h at room temperature using a dilution of 1:10,000 for anti-mouse and anti-rabbit antibodies.

Detection was performed using the iBright FL1500 imaging system (ThermoFisher Scientific) following chemiluminescence reaction. Bands were visualized using the Westar Antares HRP substrate kit (Cyanagen), consisting of a 1:1 mixture of luminol and hydrogen peroxide. Membrane images were subsequently analyzed using the iBright Analysis Software (ThermoFisher Scientific). Quantification and normalization of band intensity were performed using the Total Protein Normalization (TPN) method, which relies on the total protein content in each lane rather than housekeeping proteins. This approach allows for accurate comparison of relative protein levels across samples, generating a numerical value proportional to the intensity of each band.

Table 3. Western Blot antibodies

Antibody	ID code	Brand	Dilution	Host Specie	Molecular Weight
BCL2	13-8800	Invitrogen	1:500	Mouse	27 kDa
PLCγ2	5283	Santa Cruz	1:500	Rabbit	148 kDa
PKCα	PA5-17551	Thermo Fisher Scientific	1:1000	Rabbit	80 kDa
pPKCα	07-790	UPSTATE Biotechnology	1:500	Rabbit	80 kDa
AKT	9272	Cell Signaling Technology	1:1000	Rabbit	60 kDa
pAKT	4058	Cell Signaling Technology	1:1000	Rabbit	60 kDa
GSK3α/β	5676	Cell Signaling Technology	1:1000	Rabbit	48, 51 kDa
pGSK3α/β	8566	Cell Signaling Technology	1:1000	Rabbit	48, 51 kDa
Caspase3	9662	Cell Signaling Technology	1:1000	Rabbit	17, 19, 35 kDa
PARP	9542	Cell Signaling Technology	1:1000	Rabbit	89, 116 kDa

3.7. Statistical analysis

All statistical analyses were conducted using GraphPad Prism (version 5.0, GraphPad Software, San Diego, CA, USA). For experiments performed on cell lines, differences between groups were evaluated using the unpaired Student's *t*-test. In the case of patient-derived samples, quantitative PCR data involving comparisons across multiple groups were analyzed using one-way analysis of variance (ANOVA). Statistical significance was defined as $*p < 0.05$, $**p < 0.01$, $***p < 0.001$, and ****p<0.0001.

3.8. CRISPR-Cas9 generation of PDZD2 Knock-in models

3.8.1. Experimental Design

For CRISPR-Cas9–mediated genome editing, HEK293 cells were used as the model system. The experimental design was carried out using the Alt-R™ CRISPR homology-directed repair (HDR) Design Tool (Integrated DNA Technologies, IDT) to select optimal target sites and donor templates. Synthetic single guide RNAs (sgRNAs) were purchased from Synthego (Synthego Corporation, Redwood City, CA, USA): one sgRNA was designed for the HA-tag locus, one for the CASP3 locus, and two independent sgRNAs were designed for the NLS locus due to the larger size of the target region (Table 4). For each locus, single-stranded donor DNA templates (HDR templates) were synthesized by Integrated DNA Technologies (IDT), with both sense and antisense strands prepared and subsequently used in equimolar mix to maximize knock-in (KI) efficiency (Table 4).

Table 4. HDR templates and guide RNAs employed for PDZD2 knock-in editing

<table>
<tr><th colspan="3">HA knock-in</th></tr>
<tr><th>Primers/Guide</th><th>Sequence</th><th>Company</th></tr>
<tr><td>HDR-HA+</td><td>AGACCTCTGATGATGCTGGTGTCTGGGAGTGAGCACCATGTACCCATACGATGTTCCAGATTACGCTTACCCATACGATGTTCCAGATTACGCTCCCATCACCCAAGATAATGCCGTGCTGCATCTGCCCCTCCTCTACCAGTGGCT</td><td>IDT</td></tr>
<tr><td>HDR-HA-</td><td>AGCCACTGGTAGAGGAGGGGCAGATGCAGCACGGCATTATCTTGGGTGATGGGAGCGTAATCTGGAACATCGTATGGGTAAGCGTAATCTGGAACATCGTATGGGTACATGGTGCTCACTCCCAGACACCAGCATCATCAGAGGTCT</td><td>IDT</td></tr>
<tr><td>PDZD2 HA sgRNA 2</td><td>GTGCAGCACGGCATTGTCCT</td><td>Synthego</td></tr>
<tr><th colspan="3">NLSmut knock-in</th></tr>
<tr><th>Primers/Guide</th><th>Sequence</th><th>Company</th></tr>
<tr><td>HDR-NLSmut +</td><td>GAGTTTTGGGAACATCCCTGTTTTCGGGGACTATGGTGAAGCGGCCGCAGGGGGCGCAGCAGCGGCAACCCACCAGGGTCCTGTGCTGGATGTGGGCTGCATCTGGG</td><td>IDT</td></tr>
<tr><td>HDR-NLSmut -</td><td>CCCAGATGCAGCCCACATCCAGCACAGGACCCTGGTGGGTTGCCGCTGCTGCGCCCCCTGCGGCCGCTTCACCATAGTCCCCGAAAACAGGGATGTTCCCAAAACTC</td><td>IDT</td></tr>
<tr><td>PDZD2 NLSmut sgRNA 1</td><td>GGGACTATGGTGAAAAGCGC</td><td>Synthego</td></tr>
<tr><td>PDZD2 NLSmut sgRNA 2</td><td>AAGAAGAGGAAAACCCACCA</td><td>Synthego</td></tr>
<tr><th colspan="3">Caspase3mut knock-in</th></tr>
<tr><th>Primers/Guide</th><th>Sequence</th><th>Company</th></tr>
<tr><td>HDR-Casp3mut +</td><td>CGCTCCAAGCTCCAGGAGCTGAGAGCCTTGAGCATGCCTGCACTTGACAAGCTCTGCAGCGAGGATTACTCAGCAGGGCCGA</td><td>IDT</td></tr>
<tr><td>HDR-Casp3mut -</td><td>TCGGCCCTGCTGAGTAATCCTCGCTGCAGAGCTTGTCAAGTGCAGGCATGCTCAAGGCTCTCAGCTCCTGGAGCTTGGAGCG</td><td>IDT</td></tr>
<tr><td>PDZD2 Casp3mut sgRNA</td><td>CTGCAGAGCTTGTCAAGGTC</td><td>Synthego</td></tr>
</table>

3.8.2. Genome editing

HEK293 cells or HEK293 PDZD2 KI clones were expanded in standard culture conditions (DMEM + 10% FBS, 1% penicillin/streptomycin, 2 mM L-glutamine; 37°C, 5% CO_2) and used for genome editing at 60–80% confluence. To increase HDR efficiency, cells were synchronized by treatment with Nocodazole (NOC) at 1 ug/mL for 16 hours prior to electroporation, without release. After NOC treatment, cells were detached using 1× Trypsin and counted. For each condition, 3 × 10^5 cells were resuspended in Genome Editing Buffer (Thermo Fisher Scientific). In parallel, a fraction of NOC-treated cells was collected and processed for cell cycle analysis to confirm the efficacy of synchronization. Ribonucleoprotein (RNP) complexes were assembled immediately before electroporation by incubating recombinant Cas9 nuclease (Synthego) with the respective sgRNAs (Synthego) at a 1:6 molar ratio, as indicated in Table 5. The mixture was incubated on ice for 20 min to allow complex formation. For each targeted locus, the pre-assembled RNP was supplemented with an equimolar mix of sense and antisense HDR donor templates (IDT) at a final concentration of 500nM per condition.

Electroporation was carried out using the Neon Transfection System (Thermo Fisher Scientific), following the manufacturer's instructions at the optimized condition: 1100 V, 20 ms, 2 pulses. Immediately after electroporation, cells were transferred into a 12-well plate with 1mL of pre-warmed complete DMEM medium supplemented with 10% FBS and antibiotics, and incubated under standard culture conditions (37 °C, 5% CO_2) for 72 hours.

*Table 5. Experimental setup for genome editing experiments (*Stock is at 100uM (dilute accordingly**))*

Condition	**Cas9 (uL/cond)**	**sgRNA**	**sgRNA (uL/cond)**	**HDR template * (+ and -) 500nM/condition**
NTC	0.67	sgNTC	1.2	-
NTC	0.67	sgNTC	1.2	0.5uL of dilution**
HA	0.67	sgPDZD2 KI2	1.2	0.5uL of dilution**
NLSmut	0.67	NLSmut #1 + NLSmut #2	0.6 + 0.6	0.5uL of dilution**
Casp3mut	0.67	Cas3mut	1.2	0.5uL of dilution**

3.8.3. Cell Cycle analysis

Cell cycle profiling was performed 16 h after NOC treatment to confirm synchronization efficiency. Briefly, 50-100 uL cells were harvested, transferred to 96-well round-bottom plates, and centrifuged at 1500 rpm for 5 min. Cells were washed once with FACS buffer (3% FBS in PBS 1×) and fixed in 4% paraformaldehyde for 15 min at room temperature. After fixation, cells were washed with FACS buffer and permeabilized with 0.15% Triton X-100 in PBS for 2–5 min at room temperature. Following an additional wash, cells were stained with DAPI (0.1 mg/mL stock; final concentration 1× in 0.03% Triton X-100) for 15 min at room temperature in the dark. Stained cells were acquired on a CytoFLEX flow cytometer (Beckman Coulter), and DNA content was quantified to determine the distribution of cells across cell cycle phases. Data were analyzed using FlowJo software (BD Biosciences).

3.8.4. Clonal expansion

Clonal expansion was performed by limiting dilution to seed an average of 5 cells/well in 96-well plates. For each experimental arm (non-targeting control, HA, NLS and CASP3 edits) ten 96-well plates were prepared. Plates were incubated under standard culture conditions (37°C, 5% CO_2) for three weeks, with medium replacement once weekly. Wells were monitored by light microscopy at regular intervals and wells containing growing colonies after three weeks were selected for downstream processing. Each selected clone was split for two purposes: (i) genomic DNA extraction for genotyping and confirmation of precise knock-in events, and (ii) continued *in vitro* expansion to generate sufficient cells for functional assays and for cryopreservation. Expanded clones were cryopreserved in liquid nitrogen using standard freezing (90% FBS + 10% DMSO) medium and archived for subsequent analyses.

3.8.5. Genome Editing verification

Genomic DNA was extracted from pooled HEK293 cells, harvested 72 h post-transfection, as well as from expanded single-cell clones. DNA isolation was performed using the QIAamp DNA Mini Kit (Qiagen) for pooled cells and the Quick-DNA™ 96 Kit (Zymo Research) for clonal populations, according to the manufacturer’s protocols. DNA concentration and purity were assessed using a NanoDrop spectrophotometer (Thermo Fisher Scientific).

Target loci were amplified by PCR using locus-specific primers (exon 2 forward/reverse for NTC, HA, and NLS; exon 20 forward/reverse for CASP3), yielding amplicons of ~985 bp. PCR reactions were prepared using the FastStart High Fidelity PCR System (Roche), with reagent composition and cycling conditions summarized in Table 6 and Table 7.

Table 6. PCR reaction mix.

Reagent	Volume (uL)
FastStart HF Buffer 2 (10X)	5
10nM dNTPs	1
PDZD2 Primer mix (10uM)	1
FastStart HF Enzyme Blend	0.5
gDNA	15-75 ng
H_2O	To 50

Table 7. PCR cycling conditions.

NTC, HA and NLSmut condition			
Step	**Cycle**	**Time**	**Temperature (°C)**
Initial denaturation	1	4 min	95
Denaturation	40	30 sec	95
Annealing		30 sec	60
Elongation		1 min	72
Final elongation	1	7 min	72
Cooling		Unlimited	4
CASP3mut condition			
Step	**Cycle**	**Time**	**Temperature (°C)**
Initial denaturation	1	4 min	95
Denaturation	40	30 sec	95
Annealing		30 sec	60
Elongation		30 sec	72
Final elongation	1	5 min	72
Cooling		Unlimited	4

Following amplification, PCR products were purified using the MiniElute PCR Purification Kit (Qiagen) and stored at –20 °C until further analysis.

For KI validation, purified PCR products were prepared and submitted to Integrated DNA Technologies (IDT) for sequencing. Samples were prepared as follows: 10 µL DNA (2 ng/µL) + 5 µL forward primer (5 µM). Forward primers from exon 2 were used for NTC, HA, and NLS loci, whereas exon 20 forward primers were used for CASP3. Sequencing data were subsequently analyzed using the ICE Analysis Tool (Synthego Corporation, Redwood City, CA, USA).

4. RESULTS

4.1. *Ex vivo* Analyses in MDS Patients Treated with AZA or AZA+VEN

4.1.1. Clinical and Molecular Characterization of MDS Patients Treated with AZA or AZA + VEN

The study included 8 subjects (Table 8) newly diagnosed with MDS, classified according to the 2016 WHO criteria (152). According to the IPSS-R for MDS (16), most patients (7 out of 8) were classified as high or very-high, while one patient belonged to the intermediate-risk category. As shown in Table 8, cytogenetic analyses revealed abnormal karyotypes in 6/8 patients, with complex and high-risk features such as del(5q), del(7q), inv(2), and other structural aberrations involving chromosomes 1, 11, 16, and 20, while two patients showed normal karyotypes.

Treatment regimens included AZA monotherapy (n=4) and AZA in combination with VEN (AZA+VEN, n=4). Patients treated with AZA alone received a median of 14 treatment cycles (range 9–31), while those treated with AZA+VEN received a median of 12.5 cycles (range 11–23). Among patients treated with AZA alone, two cases achieved hematologic improvement (HI) in combination with either complete remission (CR) or marrow complete remission (mCR), whereas two patients showed a stable disease. The first documented response was observed between cycles 2 and 8, with a median of 5 cycles and the duration of response ranged from 14 to 18 cycles, with a median of 16 cycles. In contrast, all patients receiving AZA+VEN experienced a clinical response (2 CR, 1 HI and 1 mCR). In this group, responses occurred earlier, between cycles 2 and 4 (median: 2.5 cycles), and the duration of response ranged from 10 to 17 cycles, with a median of 12.5 cycles. Progression to AML was documented in only one AZA+VEN-treated patient after 20 months.

#	Age	Sex	WHO 2016	IPSS-R	Karyotipe [no Metaphases with aberration]	NGS analysis	Treatment	Total Cycles	Clinical Outcome (IWG 2006)	Time to first response (cycles)	Duration of response (months)	Time to AML evolution (months)	Cause of death
1	82	M	MDS-EB-2	VERY HIGH	8+	/	Azacitidine	31	SD, HI + mCR	8	4 (HI); 14 (mCR)	/ (not confirmed)	CACHEXIA
2	73	F	MDS-U	HIGH	del(20)(q11q13)[16]; -7 [16]	/	Azacitidine	14	HI + CR	2 (HI); 4 (CR)	3 (HI); 15 (CR)	/	COVID-19
3	84	M	MDS-MLD	VERY HIGH	del(5q)[6]; del(5q), der(7;14), -16 [13]	SF3B1 (missense, c.2098A>G, p.Lys700Glu, exon 15, VAF 48%)	Azacitidine	14	SD	NA	NA	/	NA
4	68	M	MDS-EB-2	HIGH	NORMAL	ASXL1 (missense, c.1927G>A, p.Gly643Arg, exon 13, VAF 29%); RUNX1 (nonsense, c.419G>A, p.Gln268*, exon 7, VAF 16%; frameshift, c.302_303dupCA, p.Leu102Cysfs*21, exon 4, VAF 7%); SRSF2 (missense, c.284C>A, p.Pro95His, exon 1, VAF 5%); IDH2 (missense, c.419G>A, p.Arg140Gln, exon 4, VAF 31%)	Azacitidine	9	SD	NA	NA	/	/
5	76	F	MDS-EB-1	HIGH	del(5q) [5]	/	Azacitidine + Venetoclax	13	CR	2	11	20	/
6	81	M	MDS-MLD	INTERMEDIATE	46, XY, del(6)(q21q23)[20]	U2AF1 (VAF 33%), ASXL1 (VAF 16%)	Azacitidine + Venetoclax	12	HI + CR	2 (HI); 8 (CR)	7 (HI); 3 (CR)	/	COVID-19
7	69	F	MDS-EB-1	HIGH	NORMAL	/	Azacitidine + Venetoclax	11	HI	4	14	/	NA
8	71	M	MDS-EB-1	HIGH	8+	/	Azacitidine + Venetoclax	23	mCR	3	17	/	/

*Table 8. Patients' characteristics and outcome***.** *[M, male; F, female; WHO 2016, World Health Organization 2016 classification of myeloid neoplasms; MDS, myelodysplastic neoplasms; MDS-EB-1, MDS with excess blasts-1; MDS-EB-2, MDS with excess blasts-2; MDS-U, MDS, unclassifiable; MDS-MLD, MDS with multilineage dysplasia; IPSS-R, Revised International Prognostic Scoring System; CPSS, CMML-specific Prognostic Scoring System; del, deletion; inv, inversion; der, derivative chromosome; IWG 2006, International Working Group response criteria (2006); CR, complete remission (normal blood counts and <5% marrow blasts); mCR, marrow complete remission; HI, hematologic improvement; SD, stable disease; AML, acute myeloid leukemia; NA, not available].*

4.1.2. Characterization of Baseline Mutations in HR-MDS Patients, with a Specific Focus on *BCL2* Mutational Status

Mutational analysis revealed alterations in genes commonly implicated in myeloid malignancies (Table 8). Within the AZA monotherapy group, mutations were exclusively detected in non-responders: one patient carried a *SF3B1* Lys700Glu substitution (VAF 48%), while another presented multiple co-occurring variants, including *ASXL1* Gly643Arg (VAF 29%), a *RUNX1* nonsense mutation (p.Gln268*, VAF 16%), a *RUNX1* frameshift (p.Leu102Cysfs*21, VAF 7%), *SRSF2* Pro95His (VAF 5%), and *IDH2* Arg140Gln (VAF 31%). By contrast, patients who responded to AZA did not display any detectable mutations or karyotypic abnormalities. In the AZA+VEN cohort, all responders, three patients showed no variants, while one carried concurrent *U2AF1* (VAF 33%) and *ASXL1* (VAF 16%) mutations. Additional variants affecting *EP300*, *SF3B1*, and *KMT2D* were identified through a targeted NGS panel, although these data are not reported in detail.

Of particular relevance, a novel recurrent frameshift mutation (c.245del, p.Ala82Glyfs*14) in *BCL2* was detected in 6 of 8 patients (75%), independently from the treatment, with a VAF ranging from 2.54% to 3.33% (Table 9). Copy number analysis revealed no alterations in *BCL2*. The mutation was found in 3 out of 4 patients treated with AZA, two responders and one non-responder, and in 3 out of 4 patients receiving AZA+VEN, all of whom responded. The wild-type cases included one AZA non-responder and one AZA+VEN responder (Table 9).

Table 9. Summary of BCL2 mutational status across the patient cohort analyzed.

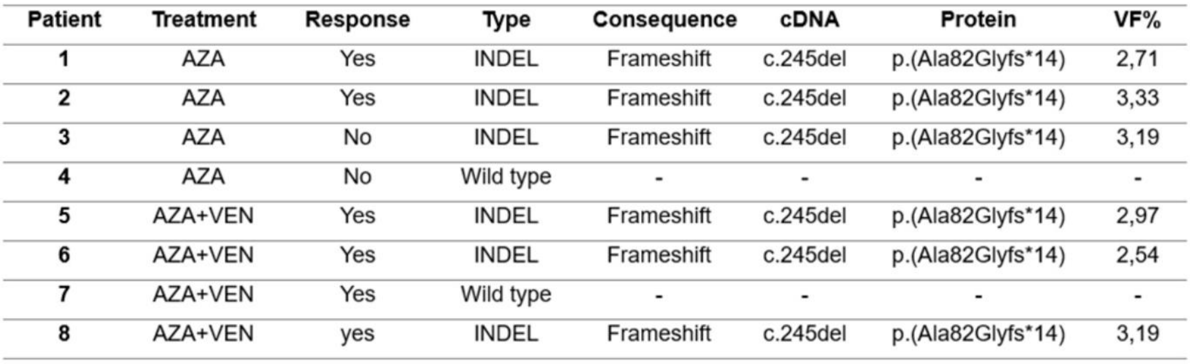

Patient	Treatment	Response	Type	Consequence	cDNA	Protein	VF%
1	AZA	Yes	INDEL	Frameshift	c.245del	p.(Ala82Glyfs*14)	2,71
2	AZA	Yes	INDEL	Frameshift	c.245del	p.(Ala82Glyfs*14)	3,33
3	AZA	No	INDEL	Frameshift	c.245del	p.(Ala82Glyfs*14)	3,19
4	AZA	No	Wild type	-	-	-	-
5	AZA+VEN	Yes	INDEL	Frameshift	c.245del	p.(Ala82Glyfs*14)	2,97
6	AZA+VEN	Yes	INDEL	Frameshift	c.245del	p.(Ala82Glyfs*14)	2,54
7	AZA+VEN	Yes	Wild type	-	-	-	-
8	AZA+VEN	yes	INDEL	Frameshift	c.245del	p.(Ala82Glyfs*14)	3,19

According to a bioinformatic analysis, the c.245del frameshift mutation (p.Ala82Glyfs*14) originates from a single-nucleotide deletion that introduces a premature stop codon, resulting in a truncated BCL2 protein of 96 amino acids. In its physiological configuration, wild-type BCL2 is organized into four conserved BCL2 homology (BH) domains, BH1 (aa 136–155), BH2 (aa 187–202), BH3 (aa 93–107), and BH4 (aa 10–30), together with a C-terminal transmembrane (TM) domain that ensures mitochondrial outer membrane anchoring and is indispensable for its anti-apoptotic function (153) (Figure 14). The cooperative action of BH1–3 domains generates the hydrophobic binding groove required for interaction with pro-apoptotic BH3-only proteins, while the BH4 domain contributes to protein stability and survival signaling pathways (153). Structural bioinformatic analyses of the mutant protein demonstrated the absence of the BH1, BH2, and TM domains, with preservation of the BH4 region and only a partial sequence of the BH3 domain (Figure 14). This domain loss is predicted to abolish the canonical anti-apoptotic activity of BCL2, thereby profoundly altering its functional properties.

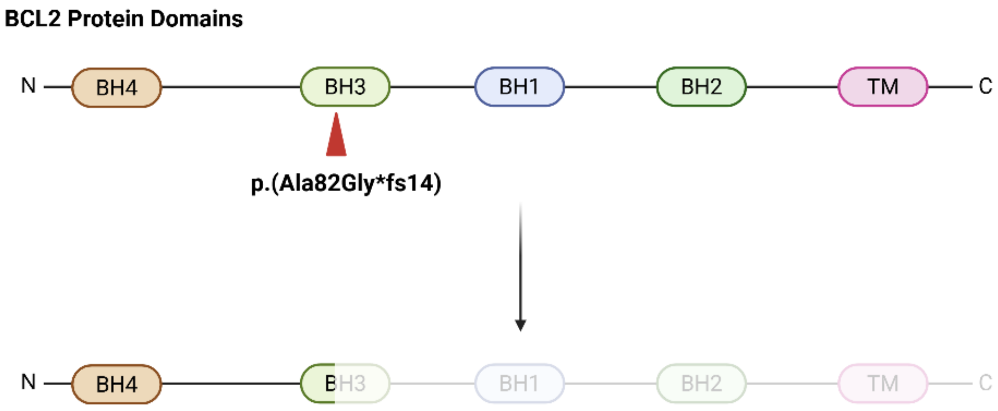

*Figure 14. Schematic representation of BCL2 depicting the canonical BH1–4 and transmembrane domains, with indication of the truncation resulting from the p.Ala82Glyfs*14 frameshift mutation.*

When stratifying patients by treatment and mutational status, we observed that 100% of our BCL2-mutated patients treated with AZA+VEN were responders, while in the AZA-only group, the response rate among BCL2-mutated patients was 66,7% (Figure 15).

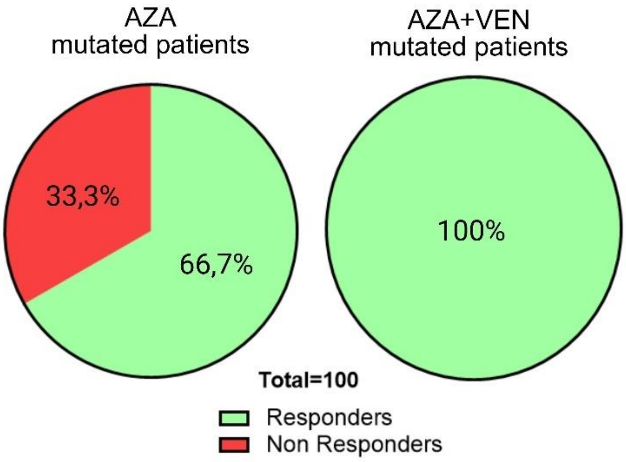

Figure 15. Pie charts showing proportion of responders among BCL2-mutated patients, showing 66.7% in the AZA monotherapy group versus 100% in the AZA+VEN combination group.

To further investigate the molecular effects of the combined AZA+VEN treatment in the context of this *BCL2* mutation, we performed a comparative analysis of gene expression at T0 and T4 in the AZA+VEN-*BCL2*-mutated cohort (Figure 16). Following treatment, *BCL2* transcript levels displayed a trend towards upregulation at T4 (6.179 ± 8.261), although this increase did not reach statistical significance. As for other molecules, a pronounced reduction was detected in the expression of genes encoding *PLCG* isoforms (*PLCG1*: 0.347 ± 0.276, $p < 0.05$ vs T0; *PLCG2*: 0.3815 ± 0.153, $p < 0.01$ vs T0), accompanied by a significant downregulation of myeloid differentiation markers (*CD11b*: 0.232 ± 0.280, $p < 0.01$ vs T0; *CD14*: 0.307 ± 0.266, $p < 0.05$ vs T0). In parallel, we observed a robust induction of pro-apoptotic regulators *BIM* (2.617 ± 0.892, $p < 0.05$ vs T0) and *BAK1* (3.909 ± 0.182, $p < 0.0001$ vs T0).

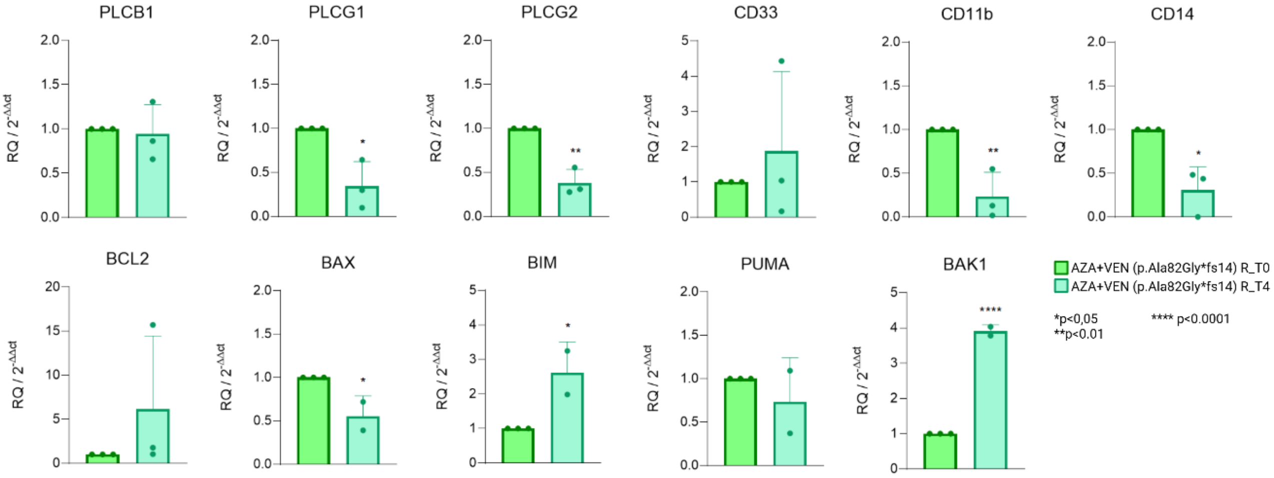

*Figure 16. qPCR assessment of gene expression for PLCB1, PLCG1, PLCG2, CD33, CD11b, CD14, BCL2, BAX, BIM, PUMA, and BAK1 in BCL2-mutated patients treated with AZA+VEN after four cycles (T4). Expression levels were normalized to GAPDH and relative to baseline (T0). Data are shown as mean ± SD. Statistical significance was evaluated using an unpaired two-tailed Student's t-test: *$p < 0.05$, **$p < 0.01$, ****$p < 0.0001$ versus T0.*

4.1.3. Gene Expression Profiles in AZA and AZA+VEN-Treated Patients

To further characterize the molecular changes linked to therapeutic response, we examined the transcriptional profiles of key signaling mediators and apoptosis-related genes dividing MDS patients according to treatment (AZA monotherapy or the AZA+VEN combination), independently of *BCL2* mutational status (Figure 17 and Figure 18).

In the AZA monotherapy cohort (Figure 17), patients who achieved a clinical response (AZA-R; blue) exhibited a pronounced induction of PLC isoforms (*PLCB1*, *PLCG1*, and *PLCG2*) as early as cycle 2 (T2), a transcriptional pattern absent in non-responders (AZA-NR; yellow). In the AZA-R cases, early treatment cycles were further characterized by an increase in the expression of myeloid differentiation markers, including *CD33*, *CD11b*, and *CD14*. By contrast, AZA-NR patients showed delayed upregulation of *CD33* and *CD11b*, which became evident only at later time points. Responders also displayed a strong and transient activation of pro-apoptotic effectors (*BAX*, *BIM*, *PUMA*, and *BAK1*) during the initial cycles, followed by a progressive reduction in transcript levels over the course of therapy (Figure 17). These molecular changes were largely absent, or markedly attenuated, in AZA-NR patients. Additionally, a modest increase of *BCL2* expression was observed at T2 in AZA-R cases.

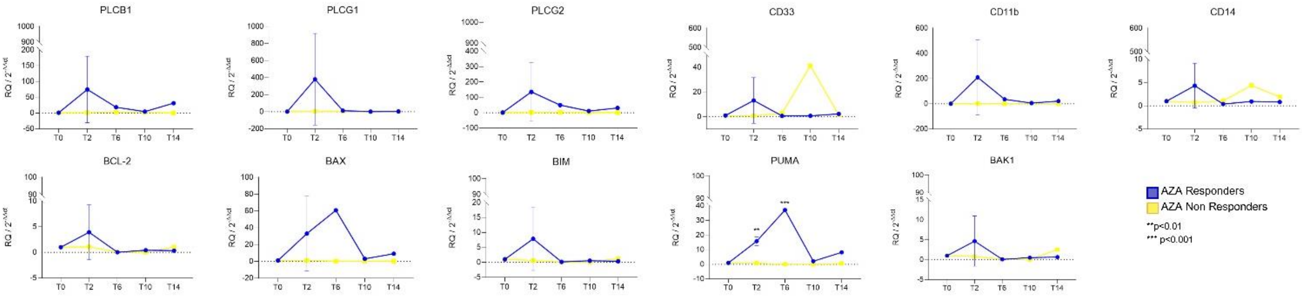

Figure 17. qPCR profiling of genes associated with PLC signaling (PLCB1, PLCG1, PLCG2), myeloid differentiation (CD33, CD11b, CD14), and apoptosis regulation (BCL2, BAX, BIM, PUMA, BAK1) in PB-MNCs from patients treated with AZA monotherapy. Samples were collected at baseline (T0) and at subsequent cycles (T2, T6, T10, T14). AZA responders (n=2) are shown in blue, and non-responders (n=3) in yellow. Gene expression is presented as mean ΔΔCt values normalized to GAPDH and baseline (T0), with SD indicated by error bars. Statistical significance was assessed using two-way ANOVA with multiple comparisons versus T0: **p < 0.01, ***p < 0.001.

In the AZA+VEN cohort (Figure 18), the transcriptional dynamics were distinct. *PLCB1* and *PLCG1* levels remained largely unchanged throughout treatment, with only minor increases at T2 and T10 for *PLCB1*, and at T6 for *PLCG1*. Conversely, *PLCG2* showed a clear induction, with peaks at T2 and T10, followed by a reduction at T14 (Figure 18). Markers of myeloid differentiation, particularly *CD33* and *CD11b*, demonstrated a progressive increase beginning at T2, reaching maximal expression at T10, and subsequently declining at T14. *CD14* followed a similar trajectory, albeit with less pronounced modulation (Figure 18). In addition, *BCL2* transcript levels rose early in AZA+VEN responders, with increased expression already detectable at T2 and maintained thereafter (Figure 18). Among pro-apoptotic genes, *BAX*, *BIM*, *PUMA*, and *BAK1* showed robust upregulation at T6, consistent with the engagement of the intrinsic apoptotic pathway under combined therapy (Figure 18).

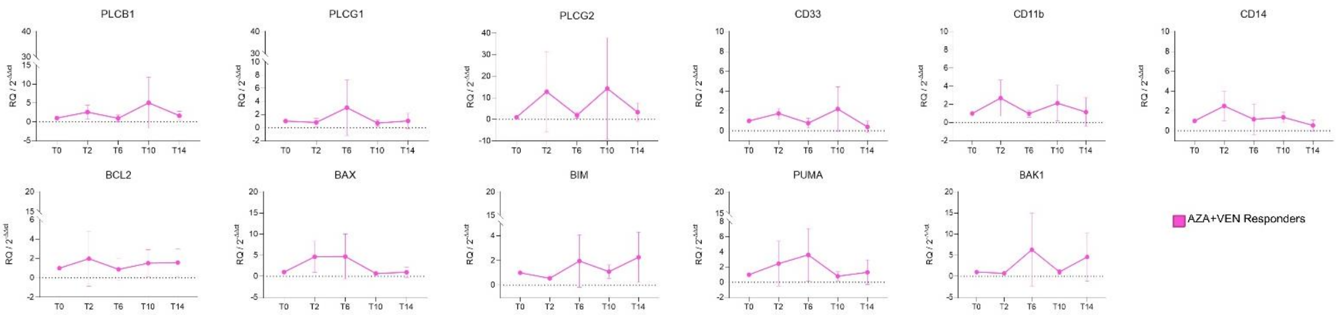

Figure 18. qPCR profiling of genes associated with PLC signaling (PLCB1, PLCG1, PLCG2), myeloid differentiation (CD33, CD11b, CD14), and apoptosis regulation (BCL2, BAX, BIM, PUMA, BAK1) in PB-MNCs from patients treated with AZA+VEN combination. Samples were collected at baseline (T0) and at subsequent cycles (T2, T6, T10, T14). AZA+VEN responders (n=4) are shown in pink. Gene expression is presented as mean ΔΔCt values normalized to GAPDH and baseline (T0), with SD indicated by error bars. Statistical significance was evaluated using two-way ANOVA with multiple comparisons against T0; all points were not significant (ns).

4.2. *In vitro* Analyses of AZA+VEN Molecular Mechanisms in Leukemic Cell Lines

To functionally validate our observations in patient samples, we next employed *in vitro* models of AML cells, as there are no reliable *in vitro* MDS models, with differential sensitivity to VEN. In particular, we used MV4-11 cells, which are highly sensitive to VEN, and THP-1 cells, which exhibit VEN resistance (154), that were treated for 24 hours with AZA (5 µM), VEN (5 nM for MV4-11; 125 nM for THP-1), or AZA+VEN.

4.2.1. Cell Cycle Analysis

Cell cycle analysis in MV4-11 cells (Figure 19A) revealed that treatment with AZA alone led to a significant increase in the proportion of cells in the sub-G0 phase (38.56% vs untreated control: 7.72%, $p < 0.01$), accompanied by a reduction in the G0/G1 (44.32% vs untreated control: 56.74%, $p < 0.05$) and G2/M (4.12% vs untreated control: 16.14%, $p < 0.001$) phases. These effects were further amplified upon combined treatment with AZA and VEN, resulting in a marked increase in sub-G0 cells (59.22% vs untreated control: 7.72%, $p < 0.0001$), and a pronounced reduction in G0/G1 (27.02% vs untreated control: 56.74%, $p < 0.0001$) and G2/M (2.62% vs untreated control: 16.14%, $p < 0.0001$) populations. In contrast, treatment with VEN alone exerted only minimal effects on cell cycle distribution, with a modest but significant increase observed in the sub-G0 phase (24.72% vs untreated control: 7.72%, $p < 0.05$), and no substantial changes in the other phases. In THP-1 cells (Figure 19B), the effects on cell cycle progression were evident only upon combined treatment with

AZA+VEN. Treatment with VEN alone resulted in a slight increase in the sub-G0 population (11.6% vs untreated control: 5.8%, $p < 0.05$), while AZA alone led to a significant reduction in the S-phase fraction (14.2% vs untreated control: 23.8%, $p < 0.01$). Notably, AZA+VEN induced a robust increase in the sub-G0 fraction (43.6% vs untreated control: 5.8%, $p < 0.0001$), along with a significant decrease in both S (10.6% vs untreated control: 23.8%, $p < 0.001$) and G2/M (4.2% vs untreated control: 22.4%, $p < 0.0001$) phases.

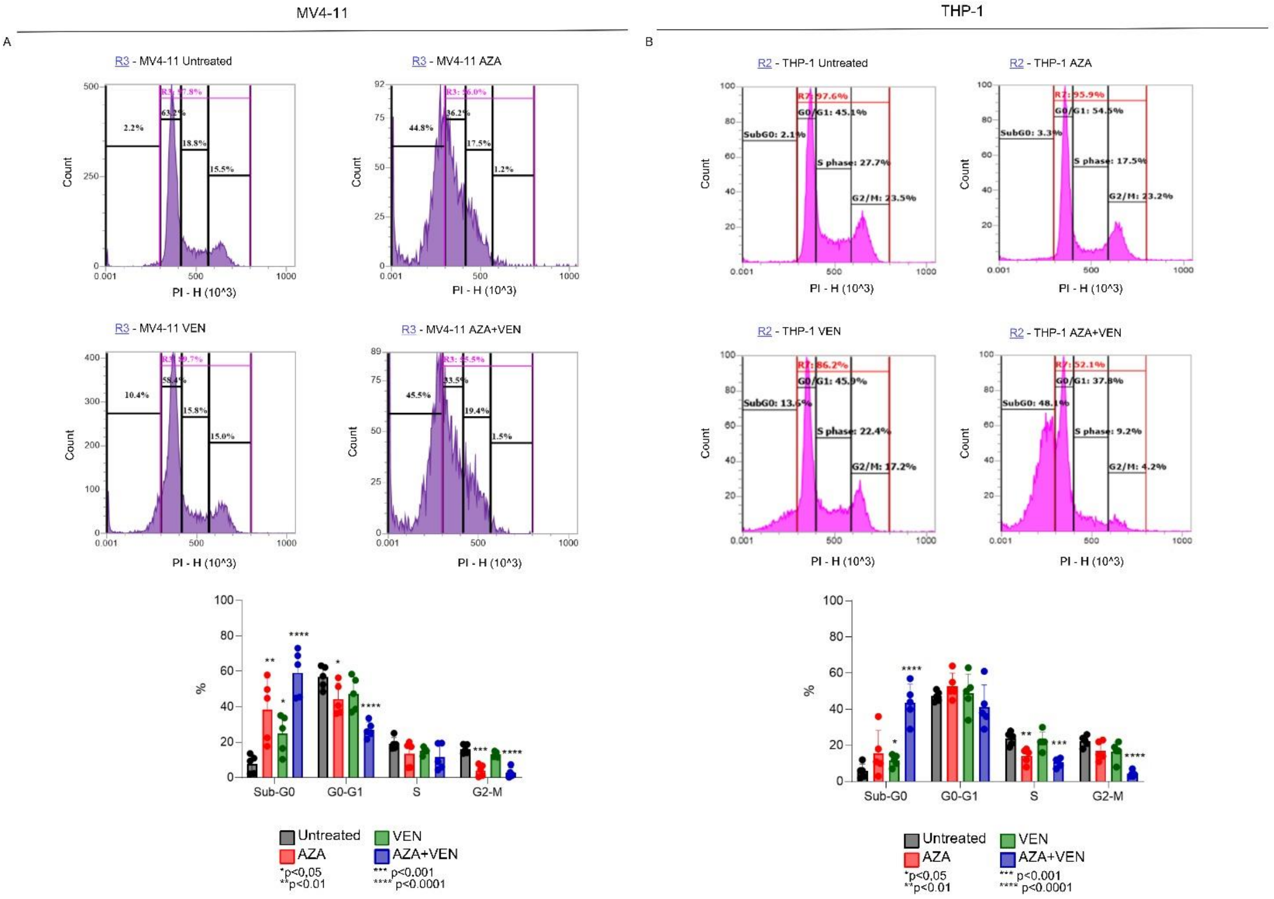

*Figure 19. Representative cell cycle distribution in MV4-11 (A) and THP-1 (B) cells following 24-hour treatment with AZA (5 µM), VEN (5 nM/125 nM), or the AZA+VEN combination. Histograms depict the proportion of cells within each phase of the cell cycle (sub-G0/G1, G0/G1, S, G2/M). Bar graphs represent mean percentages ± SD calculated from at least three independent experiments. Statistical significance was evaluated using an unpaired two-tailed Student's t test: *p < 0.05, **p < 0.01, ***p < 0.001, ****p < 0.0001 vs untreated control.*

4.2.2. Gene and Protein Expression of BCL2

To assess the modulation of BCL2, the primary molecular target of VEN, we analyzed its transcript and protein levels in MV4-11 and THP-1 cells (Figure 20). In MV4-11 cells (Figure 20A), *BCL2* showed a modest induction that was restricted to the combined AZA+VEN treatment (2.997 ± 4.625), while no significant changes were detected following AZA or VEN monotherapy. In contrast, THP-1 cells (Figure 20B) exhibited *BCL2* transcript levels comparable to untreated controls under all treatment conditions (AZA: 0.829 ± 0.369; VEN: 1.092 ± 0.131; AZA+VEN: 0.953 ± 0.345). At the protein level, Western blot analyses revealed a pronounced decrease in BCL2 in MV4-11 cells exposed to VEN, which became even more evident when cells were treated with the AZA+VEN combination (Figure 20A). In THP-1 cells, a slight reduction in BCL2 protein expression was observed, but only under the combined treatment (Figure 20B).

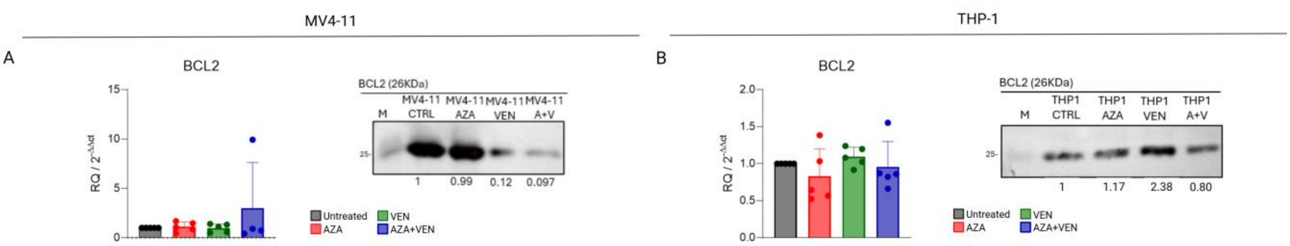

Figure 20. Analysis of BCL2 expression in MV4-11 (A) and THP-1 (B) cells by qPCR and Western blot. BCL2 mRNA levels were normalized to GAPDH and expressed relative to untreated controls. Representative Western blot images show BCL2 protein levels, with band intensity quantified using the Total Protein Normalization method. Data are presented as mean ± SD from at least three independent experiments. Statistical significance was assessed using an unpaired two-tailed.

4.2.3. Cell Death Analysis

As illustrated in Figure 19, one of the prominent effects of treatment was a notable increase in cell death, which had previously been suggested by the rise in the Sub-G0 cell cycle fraction. To further characterize the type of cell death induced by the treatments, Annexin V/PI staining was performed and analyzed via flow cytometry (Figure 21).

In MV4-11 cells (Figure 21A), exposure to either AZA or VEN alone led to a moderate decline in cell viability accompanied by an increase in apoptotic populations. Specifically, early apoptotic cells (Annexin V^{+}/PI^{-}) increased to 10.25% with AZA and 11.73% with VEN, compared to 2.58% in untreated controls, while late apoptotic/secondary necrotic cells (Annexin V^{+}/PI^{+}) rose to 40.38% and 14.50%, respectively, versus 4.88% in controls (all $p <$

0.05 vs untreated control). The combined AZA+VEN treatment elicited a substantially stronger response, reducing the viable fraction and elevating both early (15.1%) and late apoptotic cells (61.03%, $p < 0.01$ vs untreated control). Cells positive solely for PI (Annexin V^-/PI^+), indicative of primary necrosis, remained unchanged, indicating that apoptosis was the predominant mechanism.

In THP-1 cells (Figure 21B), the apoptotic effect was most pronounced under the AZA+VEN combination, which significantly decreased cell viability to 51.93% relative to 96.77% in controls ($p < 0.01$ vs untreated control) and increased both early (29.67% vs. 2.37%) and late apoptotic populations (18% vs. 0.43%, $p < 0.001$ vs untreated control). Treatment with AZA or VEN alone produced modest but statistically significant reductions in viability (AZA: 92.63%, VEN: 85.03%, $p < 0.05$ vs untreated control) along with corresponding increases in apoptotic fractions. As observed in MV4-11 cells, the proportion of Annexin V^-/PI^+ cells did not differ significantly from controls, confirming minimal involvement of primary necrosis.

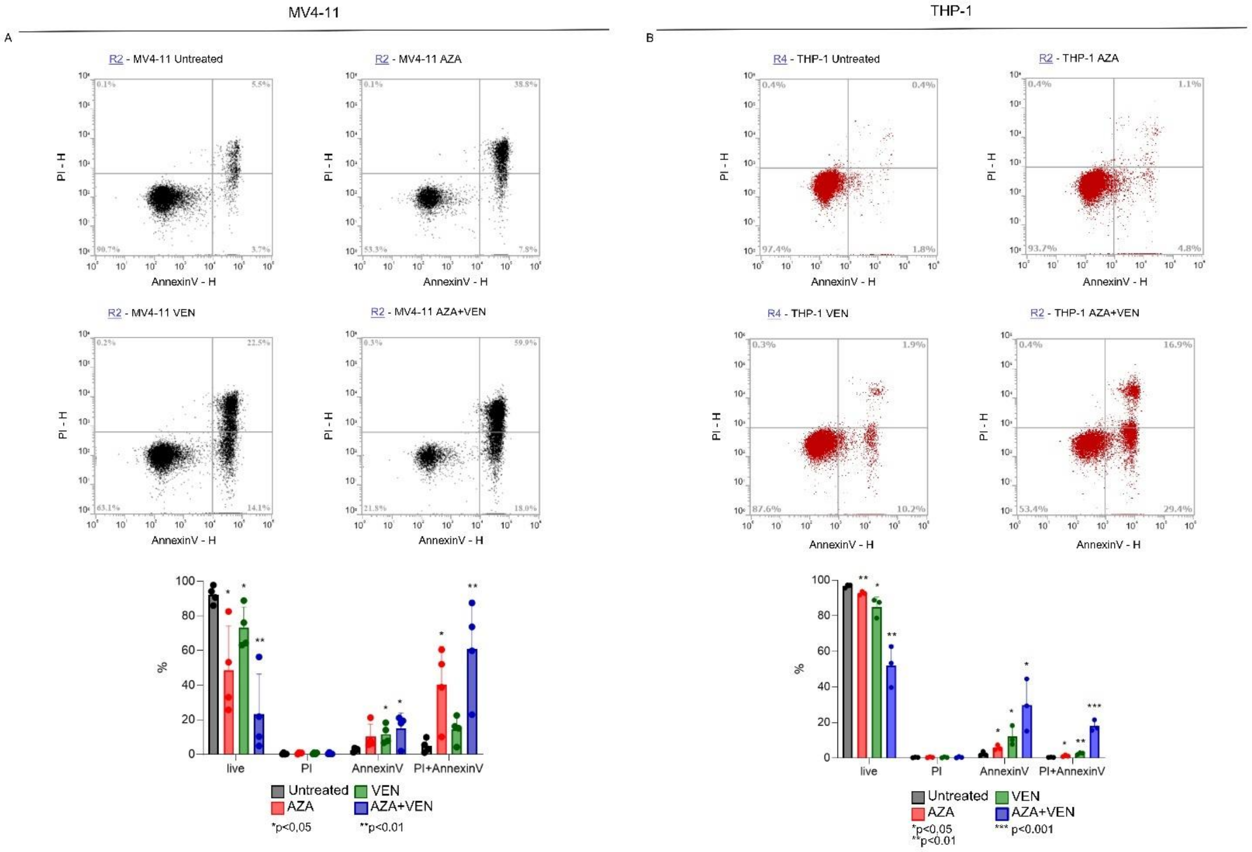

*Figure 21. Apoptotic response in MV4-11 and THP-1 cells after 24-hour treatment, evaluated by Annexin V-FITC and Propidium Iodide (PI) staining. Representative dot plots depict the distribution of viable (Annexin V–/PI–), early apoptotic (Annexin V+/PI–), late apoptotic/secondary necrotic (Annexin V+/PI+), and necrotic (Annexin V–/PI+) cell populations. Quantification of these subsets from at least three independent experiments is shown in the accompanying bar graphs. Data are expressed as mean ± SD, with statistical significance determined using an unpaired two-tailed Student's t test: *p<0.05, **p < 0.01, ***p < 0.001 vs untreated control.*

To validate the induction of apoptosis, Caspase-3 activation was assessed via Western Blot analysis. Following treatment, a reduction in the full-length Caspase-3 protein (35 kDa) was observed, while the cleaved, active fragments of Caspase-3 were not detectable (Figure 22A, B). To further investigate whether Caspase-3 activity was engaged, we examined PARP, a well-established downstream substrate of activated Caspase-3 (155). In both MV4-11 and THP-1 cells, treatment induced a decrease in the full-length PARP protein (116 kDa) accompanied by an accumulation of the cleaved form (89 kDa) (Figure 22A, B), indicating that PARP cleavage occurred as a consequence of Caspase-3-mediated apoptotic signaling.

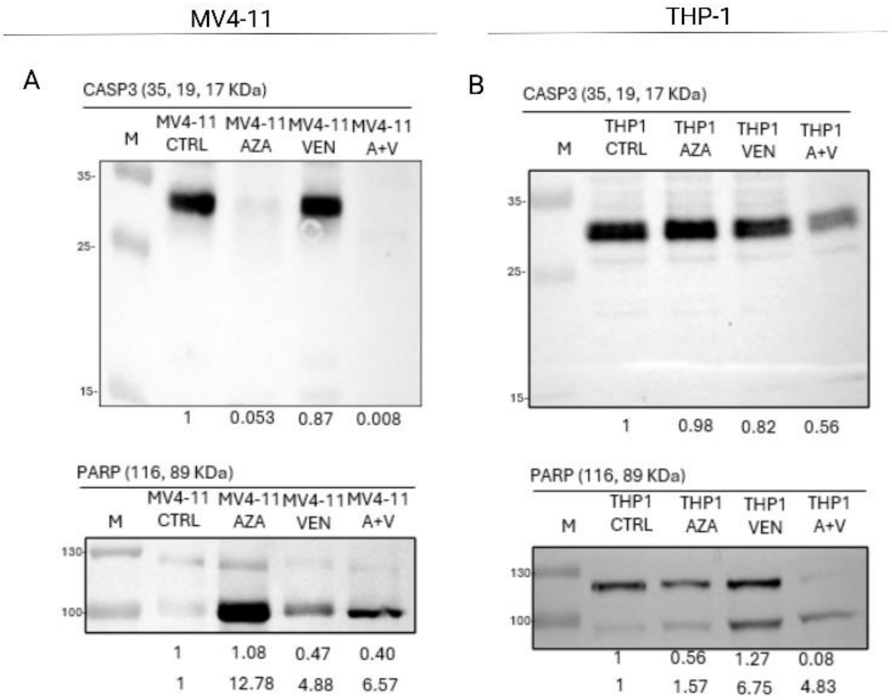

Figure 22. Western blot analysis of Caspase-3 (35/17/19 kDa) and PARP (116/89 kDa) in MV4-11 (A) and THP-1 (B) cells following 24 hours of treatment. Representative blots are shown, and band intensities were quantified relative to untreated controls using the Total Protein Normalization (TPN) method.

Lastly, we evaluated the transcriptional response of key pro-apoptotic genes (*BAX*, *BIM*, *PUMA*, *BAK1*) using quantitative qPCR (Figure 23A,B). Exposure to the AZA+VEN combination elicited a robust induction of these apoptotic mediators in both MV4-11 and THP-1 cells. Notably, *BIM* expression increased markedly (MV4-11: 28.99 ± 42.42; THP-1: 2.179 ± 0.794, $p < 0.05$ vs untreated controls), as did *BAK1* (MV4-11: 71.55 ± 107.9; THP-1: 2.765 ± 0.971, $p < 0.01$ vs untreated controls), highlighting the activation of the intrinsic apoptotic pathway in response to combined therapy.

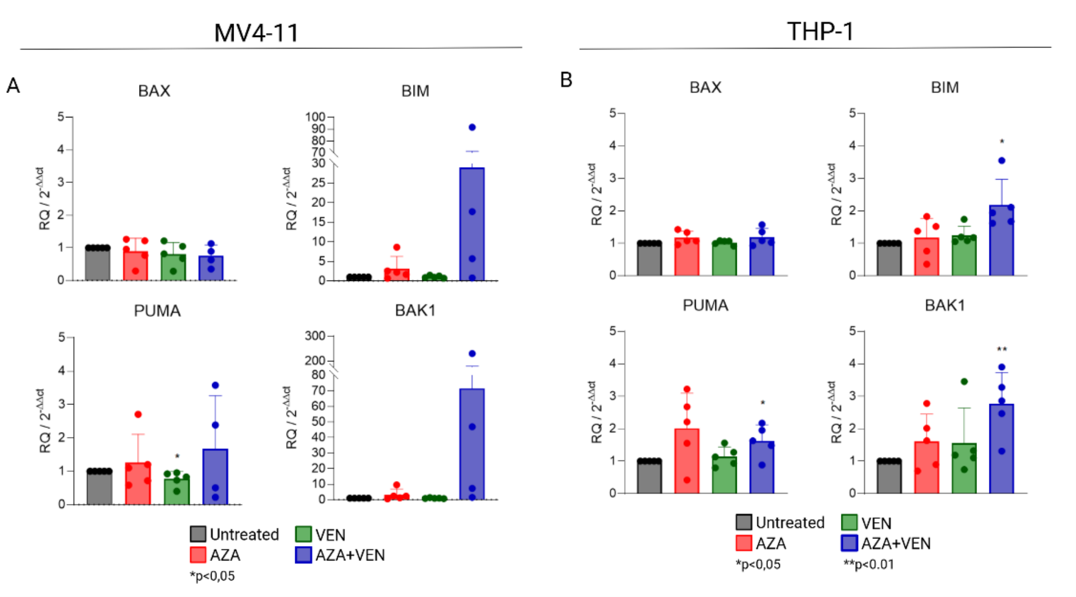

*Figure 23. Quantitative analysis of pro-apoptotic BCL2 family members genes (BAX, BIM, PUMA, BAK1) expression in MV4-11 (A) and THP-1 (B) cells following treatment. mRNA levels were measured by qPCR and normalized to GAPDH, with untreated cells serving as control. Data are presented as mean ± SD from at least three independent experiments. Statistical significance was evaluated using an unpaired two-tailed Student's t test. *p<0.05, **p<0.01 vs untreated control.*

4.2.4. Phosphoinositide (PI)-related Signaling Pathway Analyses

4.2.4.1. PLC/PKC Axis

To elucidate the molecular events associated with AZA+VEN–induced cell cycle modulation, we analyzed the expression of PLC isoforms. In VEN-sensitive MV4-11 cells, combined AZA+VEN treatment elicited a trend towards increased transcription of *PLCB1*, *PLCG1*, and *PLCG2* (Figure 24A), an effect primarily driven by AZA monotherapy. VEN alone had minimal impact on PLC expression, except for a slight reduction in *PLCB1* transcript levels (0.352 ± 0.225, $p < 0.01$ vs untreated control) (Figure 24A). In VEN-resistant THP-1 cells, *PLCB1* was significantly upregulated following AZA treatment (3.018 ± 1.481, $p < 0.05$ vs untreated control) (Figure 24B). Notably, *PLCG1* and *PLCG2* transcripts were largely unaltered by AZA or VEN monotherapies but showed significant elevation when both agents were combined (*PLCG1*: 1.889 ± 0.805, $p < 0.05$ vs untreated control; *PLCG2*: 1.441 ± 0.195, $p < 0.01$ vs untreated control) (Figure 24B). Overall, single-agent VEN exerted minimal effects on PLC transcription in both cell lines (Figure 24A,B).

At the protein level, transcriptional upregulation in MV4-11 cells did not correlate with increased PLCγ2 abundance; instead, PLCγ2 protein was markedly decreased after

AZA or AZA+VEN treatment relative to untreated controls (Figure 24C). Conversely, in THP-1 cells, PLCγ2 protein remained stable following combined therapy and was slightly elevated with either AZA or VEN alone (Figure 24D).

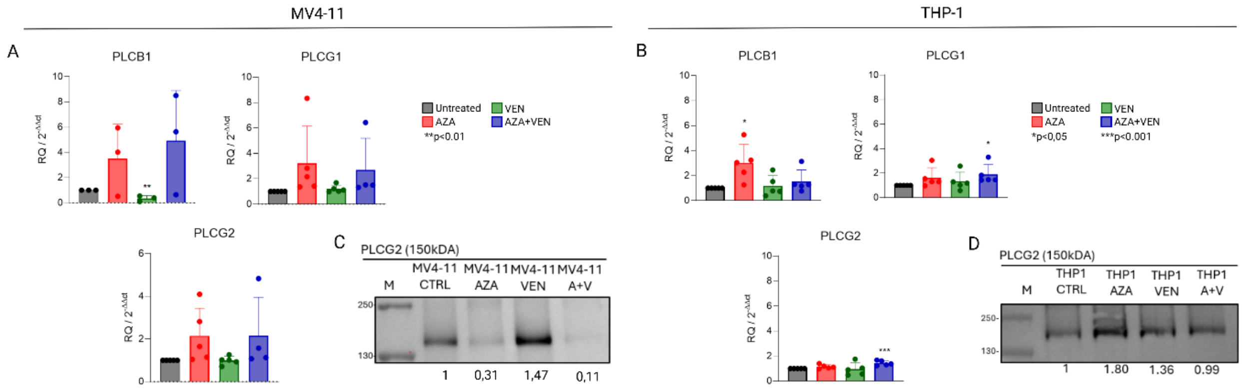

*Figure 24. (A–B) qPCR analysis of PLCB1, PLCG1, and PLCG2 transcript levels in MV4-11 (A) and THP-1 (B) cells following 24-hour exposure to AZA (5 µM), VEN (5/125 nM), or the combined AZA+VEN treatment. Expression values were normalized to GAPDH and compared to untreated controls. Data represent mean ± SD from at least three independent experiments. Statistical significance was calculated using an unpaired two-tailed Student's t test. *p<0.05, **p<0.01, ***p<0.001 vs untreated control. (C–D) Representative Western blot images showing PLCG2 protein levels in whole-cell lysates, with band intensity quantified using the Total Protein Normalization (TPN) method.*

We next examined downstream signaling by assessing PKCα activation. In MV4-11 cells, total PKCα levels remained largely unchanged, whereas phosphorylated PKCα (pPKCα) was substantially increased after AZA and AZA+VEN exposure (Figure 25A). In THP-1 cells, total PKCα was elevated, but pPKCα decreased following combined treatment (Figure 25B), indicating cell type–specific responses within the PKC signaling cascade to the same therapeutic intervention.

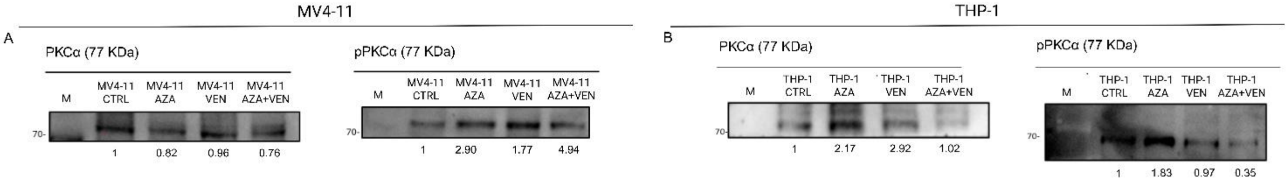

Figure 25. Representative Western blot images showing total PKCα (80 kDa) and phosphorylated PKCα (pPKCα, Thr638, 80 kDa) in MV4-11 (A) and THP-1 (B) cells following treatment. Protein band intensities were quantified using TPN method and normalized to untreated controls.

4.2.4.2. AKT/GSK3 Axis

To dissect the impact of AZA, VEN, and their combination on the AKT/GSK3 signaling cascade, we performed Western blot analyses in both cell models. In VEN-sensitive MV4-11 cells**,** treatment with AZA alone or in combination with VEN led to a pronounced reduction in total AKT levels and Ser473 phosphorylation, whereas VEN as a single agent produced no appreciable effect (Figure 26A, left panel). In VEN-resistant THP-1 cells, a similar downregulation of total and phosphorylated AKT was observed exclusively following the combined AZA+VEN regimen (Figure 26A, right panel).

We then focused on GSK3 isoforms to evaluate downstream signaling dynamics. In MV4-11 cells, both AZA and AZA+VEN markedly decreased total GSK3α and GSK3β protein levels. Interestingly, phosphorylated GSK3α was elevated under these conditions, while phosphorylated GSK3β remained undetectable, suggesting that GSK3β predominantly remains in its active, unphosphorylated form after treatment (Figure 26B, left panel). In THP-1 cells, total GSK3α and GSK3β levels remained largely unchanged, with only a minor increase in pGSK3α detected upon treatment. Notably, phosphorylated GSK3β was absent across all conditions, including untreated controls, indicating a baseline lack of GSK3β phosphorylation in this model (Figure 26B, right panel).

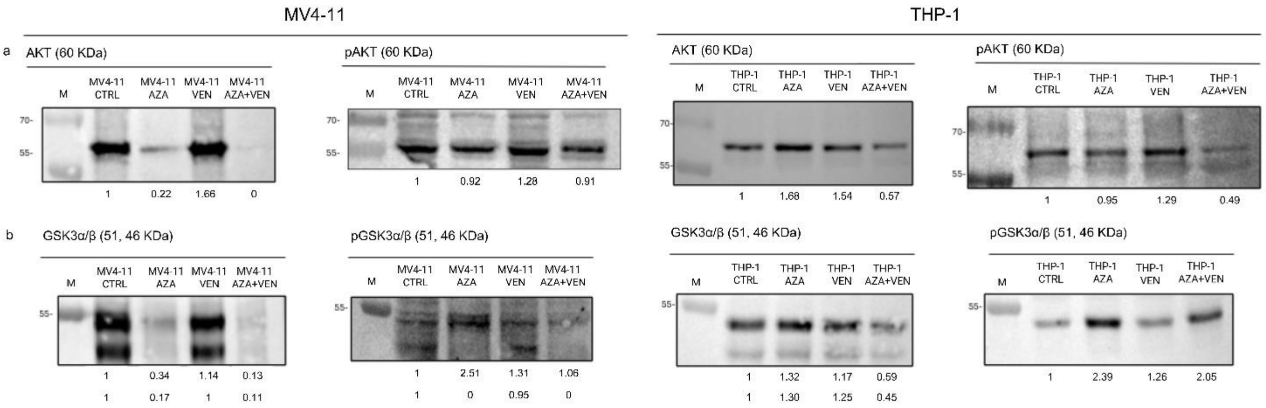

Figure 26. Representative Western blot images depicting total AKT (60 kDa) and phosphorylated AKT (Ser473) (A), as well as total GSK3α/β (51/46 kDa) and phosphorylated GSK3α/β (Ser21/Ser9) (B) in MV4-11 (left panels) and THP-1 (right panels) cells following 24-hour treatment with AZA (5 μM), VEN (5/125 nM), or their combination (AZA+VEN). Protein band intensities were quantified using the TPN method and normalized to untreated controls.

4.2.5. Myeloid Differentiation Markers Expression Analysis

Given the established involvement of PLC/PKC signaling in the regulation of hematopoietic differentiation (129,156), we analyzed the transcriptional levels of key myeloid surface markers by quantitative PCR (Figure 27A,B) . In MV4-11 cells, *CD33* expression was significantly elevated following AZA monotherapy (1.796 ± 0.562, $p < 0.05$ vs untreated control) and upon combined AZA+VEN treatment (2.711 ± 1.435, $p < 0.05$ vs untreated control), suggesting expansion of early myeloid progenitors. *CD11b* transcript levels did not show substantial variations under any treatment condition. *CD14* was upregulated by both AZA (3.384 ± 1.842, $p < 0.05$ vs untreated control) and VEN (1.645 ± 0.606, $p < 0.05$ vs untreated control) alone, whereas the combination therapy induced a non-significant increase (Figure 27A). In THP-1 cells, a modest, yet statistically significant, increase in *CD33* was observed only with AZA+VEN (1.587 ± 0.454, $p < 0.05$ vs untreated control). *CD11b* (2.058 ± 0.350, $p < 0.001$ vs untreated control) and *CD14* (7.095 ± 3.614, $p < 0.01$ vs untreated control) were strongly induced by AZA alone, with *CD14* levels remaining elevated following combination treatment (4.814 ± 1.463, $p < 0.001$ vs untreated control) (Figure 27B).

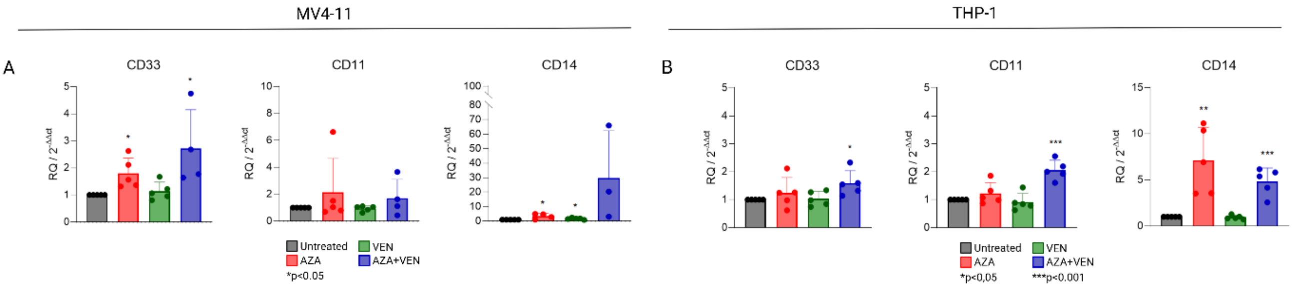

*Figure 27. qPCR analysis of myeloid differentiation markers CD33, CD11b, and CD14 in MV4-11 (A) and THP-1 (B) cells. Data are expressed as mean ± SD from at least three independent experiments. Statistical significance was assessed using an unpaired two-tailed Student's t test. *p<0.05, **p<0.01, ***p<0.001 vs untreated control.*

4.3. Generation of PDZD2 Knock-In models

4.3.1. Insertion of the first modification

To introduce precise modifications in the *PDZD2* locus, three site-specific edits were targeted within a single genome editing workflow: (i) insertion of an N-terminal HA epitope tag, (ii) introduction of a single-nucleotide substitution at the canonical Caspase-3 (CASP3) cleavage site, and (iii) alteration of the NLS signal.

To enhance HDR efficiency, HEK293 cells were synchronized using nocodazole (NOC). After 16 hours of treatment, cell cycle analysis revealed a redistribution of cells, with untreated controls showing 52.0% in G1, 11.5% in S, and 23.3% in G2-M, whereas NOC-treated cells accumulated predominantly in G2-M (50.3%), accompanied by a reduction in G1 (15.4%) and a modest increase in S phase (17.3%) (Figure 28).

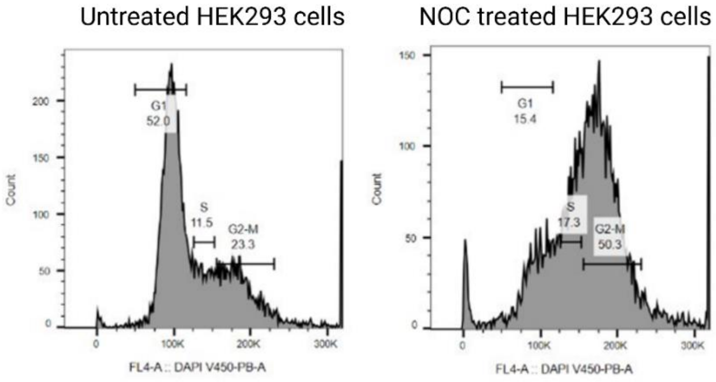

	G1	**S**	**G2-M**
Untreated HEK293 cells	52%	11,5%	23,3%
NOC treated HEK293 cells	15,4%	17,3%	50,3%

Figure 28. Representative histograms showing cell cycle distribution of HEK293 cells following 16-hour nocodazole (NOC) treatment. The accompanying table summarizes the percentage of cells in G1, S, and G2-M phases for both untreated controls and NOC-treated samples.

Subsequently, synchronized cells were electroporated with the three KI constructs. 72 hours post-electroporation, targeted sequencing revealed differential editing outcomes: the CASP3 construct achieved a 13% knock-in rate, while the HA-tag construct reached only 2%. In contrast, analysis of the NLS construct demonstrated a high frequency of indels, with 94% of alleles carrying knockout-type mutations (Figure 29).

SUCCESSFULLY ANALYZED SAMPLES

SAMPLE ⓘ	GUIDE TARGET ⓘ	NUCLEASE ⓘ	INDEL % ⓘ	MODEL FIT (R²) ⓘ	KNOCK... SCORE ⓘ	KNOCK... SCORE ⓘ	
NLS-E2_F	AAGAAGAGGAAAACCCACCA GGGACTATGGTGAAAAGCGC	SPCAS9	94	0.77	94		View Details
CASP3-E20_F	CTGCAGAGCTTGTCAAGGTC	SPCAS9	76	0.95		13	View Details
HA-E2_F	GTGCAGCACGGCATTGTCCT	SPCAS9	75	0.92		2	View Details

HA pooled cells

Status ⓘ	Guide Target ⓘ	PAM Sequence ⓘ	Indel % ⓘ	Model Fit (R²) ⓘ	Knockin-Score ⓘ	Nuclease ⓘ
Succeeded	GTGCAGCACGGCATTGTCCT	GGG	75	0.92	2	spcas9

CASP3 mut pooled cells

Status ⓘ	Guide Target ⓘ	PAM Sequence ⓘ	Indel % ⓘ	Model Fit (R²) ⓘ	Knockin-Score ⓘ	Nuclease ⓘ
Succeeded	CTGCAGAGCTTGTCAAGGTC	AGG	76	0.95	13	spcas9

Figure 29. Assessment of PDZD2 K efficiency in pooled HEK293 cells 72 hours post-electroporation. The bar graph (top) represents the percentage of indels (blue), KO (green) and KI events (red) for NLS, CASP3, and HA constructs. The table summarizes editing outcomes, including indel frequency, model fit, and KI scores for each target. Below, sequence alignments illustrate the distribution of edited alleles in pooled HA-tagged and CASP3-mutant cells, highlighting successful KI events.

To evaluate the stability of edits at the clonal level, single-cell cloning was performed following three weeks of culture, resulting in the isolation of 13 Non-Targeting Control (NTC)-derived clones, 20 HA-tag clones, and 56 CASP3-mutated clones. Among the CASP3-modified population, two clones (#2 and #36) exhibited complete (100%) KI, consistent with biallelic homozygous integration. One additional clone (#55) displayed a KI score of 69%, indicative of heterozygous editing, while four other clones (#10, #19, #40, and #25) demonstrated high KI efficiencies ranging from 70% to 75% (Figure 30).

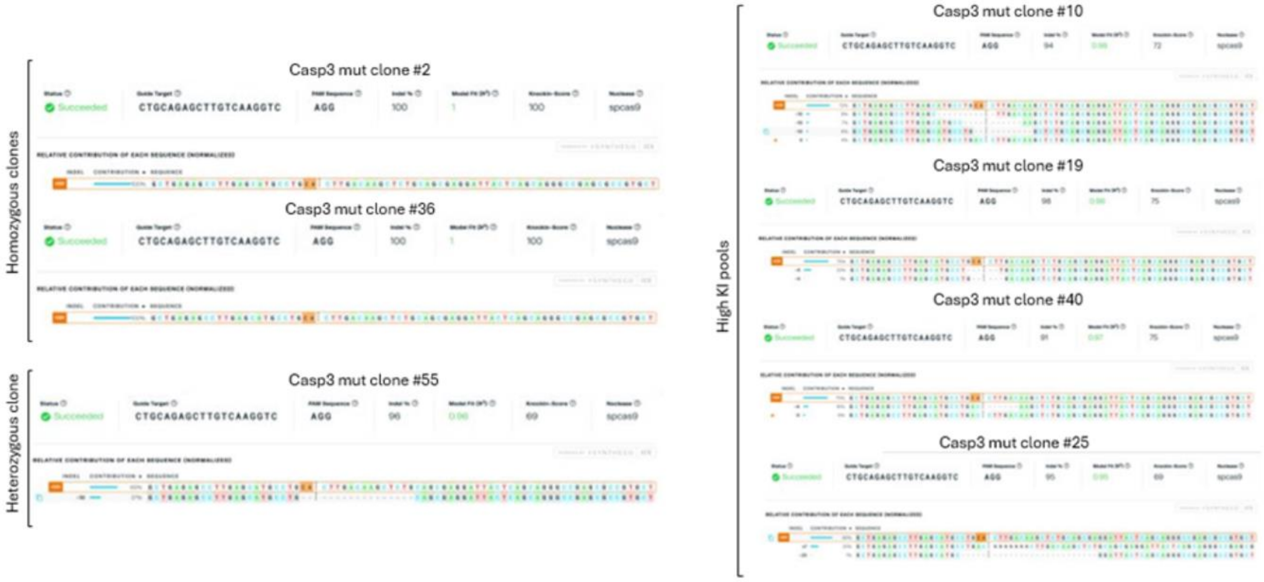

Figure 30. Targeted sequencing analysis of PDZD2 KI efficiency in clonal HEK293 cell lines. Representative sequencing results of individual CASP3-mutant HEK293 clones following HDR-mediated KI. Two clones (#2 and #36) exhibited complete biallelic (100%) KI, consistent with homozygous integration. Clone #55 showed partial (69%) KI, indicative of heterozygous integration. In addition, four independent clones (#10, #19, #40, and #25) displayed high KI efficiencies ranging from 70% to 75%.

4.3.2. Secondary insertion of the HA tag in pre-edited clones

To explore the feasibility of sequential editing, an N-terminal HA tag was introduced into clones already carrying homozygous CASP3 edits. Two CASP3 homozygous clones (#2 and #36) and one NTC clone (#7) were selected for these experiments.

As an initial step, the impact of NOC treatment on the cell cycle was reassessed in these clonal lines. After 16 hours of exposure, all clones displayed an enrichment of cells in G2-M phase, consistent with efficient synchronization. Specifically, the NTC#7 clone showed 17.1% of cells in G1, 12.5% in S, and 52.9% in G2-M. CASP3mut clone #2 exhibited 17.4% in G1, 14.5% in S, and 58.5% in G2-M, while CASP3mut clone #36 displayed 21.3% in G1, 15.1% in S, and 51.1% in G2-M (Figure 31).

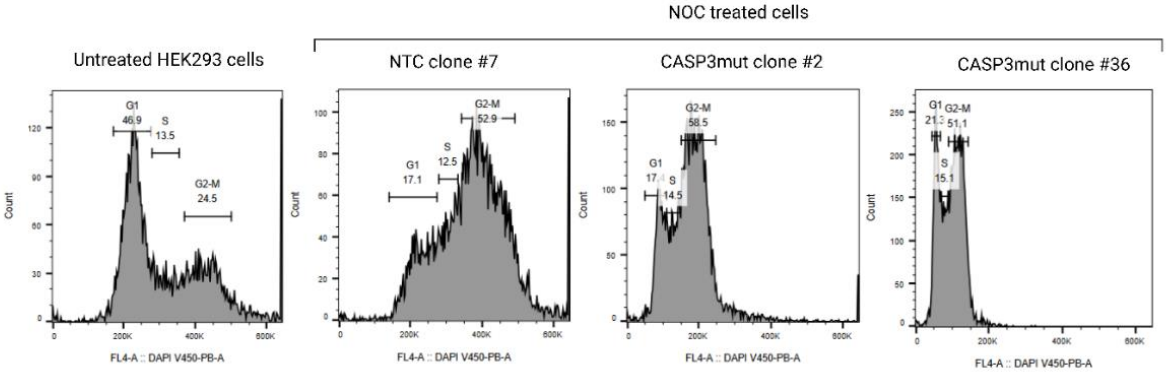

	G1	S	G2-M
Untreated HEK293 cells	46,9%	13,5%	24,5%
NTC clone#7 (NOC treated)	17,1%	12,5%	52,9%
CASP3mut clone#2 (NOC treated)	17,4%	14,5%	58,5%
CASP3mut clone#36 (NOC treated)	21,3%	15,1%	51,1%

Figure 31. Representative histograms showing cell cycle distribution of HEK293 KI clones following 16-hour nocodazole (NOC) treatment. The accompanying table summarizes the percentage of cells in G1, S, and G2-M phases for both untreated controls and NOC-treated samples.

Following electroporation with the HA construct, KI efficiency was again found to be low. In the NTC#7 clone, the HA KI frequency reached 3%, while in CASP3mut clone #2 it was limited to 1%. No KI events were detected in CASP3mut clone #36 (Figure 32).

SUCCESSFULLY ANALYZED SAMPLES

SAMPLE	GUIDE TARGET	NUCLEASE	INDEL %	MODEL FIT (R²)	KNOC... SCORE	KNOC... SCORE	
C36_HA-E2_F	GTGCAGCACGGCATTGTCCT	SPCAS9	74	0.93		0	View Details
C2_HA-E2_F	GTGCAGCACGGCATTGTCCT	SPCAS9	71	0.85		1	View Details
NTC7_HA-E2_F	GTGCAGCACGGCATTGTCCT	SPCAS9	73	0.91		3	View Details

Figure 32. Assessment of PDZD2 KI efficiency in HEK293 KI clones 72 hours post-electroporation. The bar graph (top) represents the percentage of indels (blue), KO (green) and KI events (red) for HA constructs. The table summarizes editing outcomes, including indel frequency, model fit, and KI scores for each target. Below, sequence alignments illustrate the distribution of edited alleles in pooled HA-tagged and CASP3-mutant cells, highlighting successful KI events.

After three weeks of culture, single-cell cloning was performed from the HA KI attempts. From the NTC#7HA pool, 7 clones were successfully isolated, while no viable clones could be recovered from the CASP3#2HA pool. Sequencing analysis of the NTC#7HA-derived clones could not be completed due to the limited number of cells, which precluded robust evaluation. Furthermore, re-analysis of the bulk NTC#7HA pool revealed complete loss of the HA KI over time: while a KI frequency of 3% had been detected at 72 hours, the modification was no longer detectable after three weeks, with efficiency declining to 0% (Figure 33).

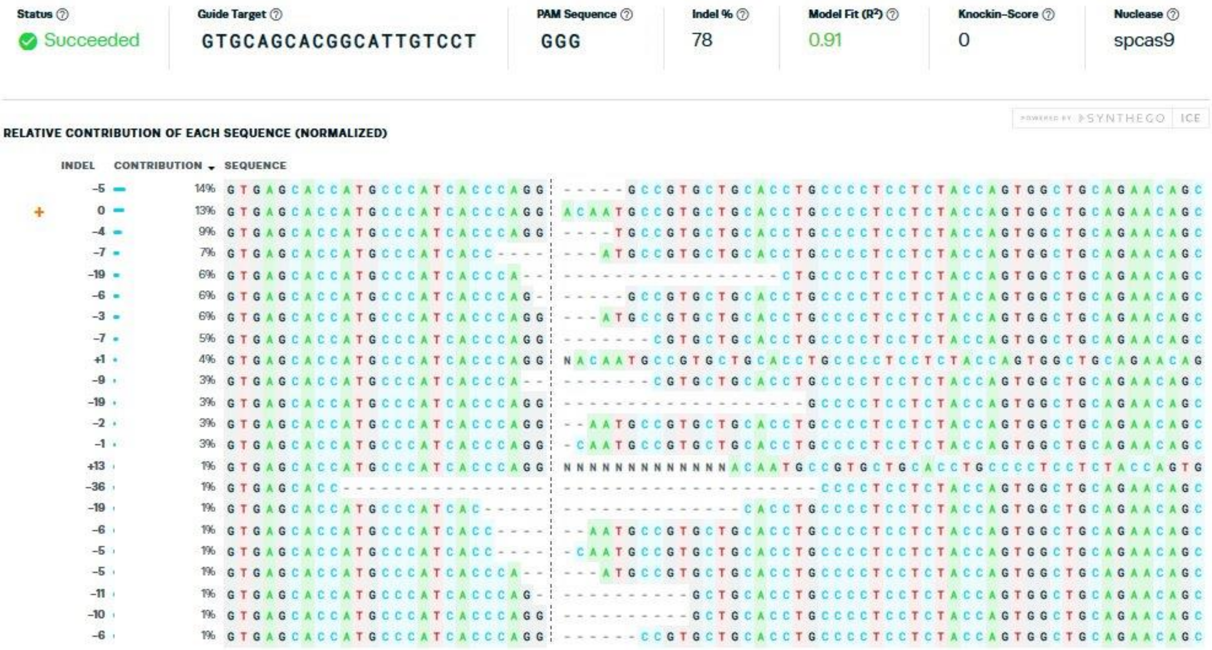

Status	Guide Target	PAM Sequence	Indel %	Model Fit (R^2)	Knockin-Score	Nuclease
Succeeded	GTGCAGCACGGCATTGTCCT	GGG	78	0.91	0	spcas9

RELATIVE CONTRIBUTION OF EACH SEQUENCE (NORMALIZED)

	INDEL	CONTRIBUTION	SEQUENCE	
	-5	14%	GTGAGCACCATGCCCATCACCCAGG	-----GCCGTGCTGCACCTGCCCCTCCTCTACCAGTGGCTGCAGAACAGC
+	0	13%	GTGAGCACCATGCCCATCACCCAGG	ACAATGCCGTGCTGCACCTGCCCCTCCTCTACCAGTGGCTGCAGAACAGC
	-4	9%	GTGAGCACCATGCCCATCACCCAGG	----TGCCGTGCTGCACCTGCCCCTCCTCTACCAGTGGCTGCAGAACAGC
	-7	7%	GTGAGCACCATGCCCATCACC----	---ATGCCGTGCTGCACCTGCCCCTCCTCTACCAGTGGCTGCAGAACAGC
	-19	6%	GTGAGCACCATGCCCATCACCCA--	-----------------CTGCCCCTCCTCTACCAGTGGCTGCAGAACAGC
	-6	6%	GTGAGCACCATGCCCATCACCCAG-	-----GCCGTGCTGCACCTGCCCCTCCTCTACCAGTGGCTGCAGAACAGC
	-3	6%	GTGAGCACCATGCCCATCACCCAGG	---ATGCCGTGCTGCACCTGCCCCTCCTCTACCAGTGGCTGCAGAACAGC
	-7	5%	GTGAGCACCATGCCCATCACCCAGG	-------CGTGCTGCACCTGCCCCTCCTCTACCAGTGGCTGCAGAACAGC
	+1	4%	GTGAGCACCATGCCCATCACCCAGG	NACAATGCCGTGCTGCACCTGCCCCTCCTCTACCAGTGGCTGCAGAACAG
	-9	3%	GTGAGCACCATGCCCATCACCCA--	-------CGTGCTGCACCTGCCCCTCCTCTACCAGTGGCTGCAGAACAGC
	-19	3%	GTGAGCACCATGCCCATCACCCAGG	-------------------GCCCCTCCTCTACCAGTGGCTGCAGAACAGC
	-2	3%	GTGAGCACCATGCCCATCACCCAGG	--AATGCCGTGCTGCACCTGCCCCTCCTCTACCAGTGGCTGCAGAACAGC
	-1	3%	GTGAGCACCATGCCCATCACCCAGG	-CAATGCCGTGCTGCACCTGCCCCTCCTCTACCAGTGGCTGCAGAACAGC
	+13	1%	GTGAGCACCATGCCCATCACCCAGG	NNNNNNNNNNNNNACAATGCCGTGCTGCACCTGCCCCTCCTCTACCAGTG
	-36	1%	GTGAGCACC----------------	--------------------CCCCTCCTCTACCAGTGGCTGCAGAACAGC
	-19	1%	GTGAGCACCATGCCCATCAC-----	--------------CACCTGCCCCTCCTCTACCAGTGGCTGCAGAACAGC
	-6	1%	GTGAGCACCATGCCCATCACC----	--AATGCCGTGCTGCACCTGCCCCTCCTCTACCAGTGGCTGCAGAACAGC
	-5	1%	GTGAGCACCATGCCCATCACC----	-CAATGCCGTGCTGCACCTGCCCCTCCTCTACCAGTGGCTGCAGAACAGC
	-5	1%	GTGAGCACCATGCCCATCACCCA--	---ATGCCGTGCTGCACCTGCCCCTCCTCTACCAGTGGCTGCAGAACAGC
	-11	1%	GTGAGCACCATGCCCATCACCCAG-	----------GCTGCACCTGCCCCTCCTCTACCAGTGGCTGCAGAACAGC
	-10	1%	GTGAGCACCATGCCCATCACCCAGG	----------GCTGCACCTGCCCCTCCTCTACCAGTGGCTGCAGAACAGC
	-6	1%	GTGAGCACCATGCCCATCACCCAGG	------CCGTGCTGCACCTGCCCCTCCTCTACCAGTGGCTGCAGAACAGC

Figure 33. Assessment of PDZD2 KI efficiency in HEK293 NTC#7-HA pooled cells after 3 weeks in culture. The table summarizes editing outcomes, including indel frequency, model fit, and KI scores for each target. Below, sequence alignments illustrate the distribution of edited alleles in pooled HA-tagged cells, highlighting successful KI events, if present.

5. DISCUSSION

MDS and AML are hematologic malignancies characterized by ineffective hematopoiesis, impaired differentiation of HSCs and profound epigenetic dysregulation. These alterations underlie disease heterogeneity and contribute to therapy resistance and leukemic progression, highlighting the need for mechanistic insights that can guide therapeutic innovation.

AZA and VEN represent a promising therapeutic strategy in HR-MDS; however, the precise molecular mechanisms driving their combinatorial activity remain largely unknown. Prior research has identified genetic alterations that influence response or confer resistance to VEN-based regimens in MDS and AML (65,157,158). For instance, *BAX* mutations, which disrupt the C-terminal α9 helix required for mitochondrial localization, occur in ~17% of relapsed AML patients after AZA+VEN therapy and contribute to acquired resistance, while they are absent in primary refractory cases (159,160). In contrast, *BCL2* mutations are rare in MDS and AML. Although BH3-domain–disrupting variants, such as G101V and D103Y reported in CLL, could theoretically impair VEN binding, they have not been detected in relapsed or refractory AML, highlighting the context-dependent nature of BCL2-mediated resistance (160,161).

In our study, a recurrent frameshift mutation in *BCL2* was detected in a subset of HR-MDS patients. This mutation is caused by a single nucleotide deletion that introduces a premature stop codon, generating a truncated protein of only 96 amino acids. The resulting protein lacks the BH1, BH2, and transmembrane domains, retaining only the BH4 domain and part of the BH3 region. Since VEN functions as a BH3-mimetic, selectively interacting with the BH3-binding groove of full-length BCL2 to inhibit its anti-apoptotic activity, this truncation was expected to prevent VEN binding and abrogate the protein's function. Interestingly, the mutation was present in both AZA-only and AZA+VEN treatment groups. Among patients receiving AZA alone, the observed response rate of 66.7% aligned with previously reported outcomes for this population. Surprisingly, all *BCL2*-mutated patients treated with the combination therapy achieved complete responses. This finding indicates that AZA+VEN can induce therapeutic effects even when the canonical VEN target is severely disrupted, suggesting the involvement of alternative or compensatory mechanisms. Considering the low variant allele frequency (VAF: 2–3%) of the *BCL2*-mutated clone, coexisting *BCL2*–wild-type subclones are likely to persist, allowing VEN to act canonically, while AZA+VEN may exert additional BCL2-independent effects in mutated subclones. These observations challenge the current paradigm that VEN efficacy is strictly dependent on an intact BH3-binding site. It is possible that the remaining portion of BH3 retains some capacity for atypical interactions, which may influence downstream signaling pathways. Alternatively, VEN might exert pro-apoptotic activity indirectly, for example by inhibiting other anti-apoptotic BCL2 family members. In parallel, AZA-induced epigenetic reprogramming may enhance apoptotic priming, compensating for the absence of full-length BCL2 and facilitating cell death. It is important to emphasize that the primary aim of our study was not to determine whether VEN completely loses binding to the truncated BCL2 protein. Rather, we focused on the broader signaling networks affected by AZA and VEN, independent of *BCL2* mutational status. Understanding these compensatory or adaptive pathways may indeed be critical for refining therapeutic strategies and may provide novel insights into mechanisms of sensitivity and resistance in myeloid malignancies. Future biochemical, structural, and functional studies will therefore be essential to clarify whether the observed responses arise from residual VEN–BCL2 interactions or from more global rewiring of apoptotic dependencies.

Several studies have begun to clarify the molecular basis of AZA and VEN synergy in MDS and AML. Key mechanisms include coordinated inhibition of anti-apoptotic proteins through BCL2 blockade and MCL1 downregulation (61,71), induction of NOXA by AZA to prime cells for apoptosis (70,162), disruption of mitochondrial metabolism (68), and modulation of immune and oxidative stress pathways (72). Nevertheless, the complexity of response and resistance suggests that additional regulatory layers remain uncharacterized. We therefore focused on the interplay between apoptotic programs and other signaling networks, including phosphoinositide-dependent cascades and survival pathways, which are known to influence MDS biology and treatment outcomes.

Aberrant inositide-dependent signaling, encompassing PLC/PKC and AKT/GSK3 pathways, has been implicated in MDS and AML progression, as well as in modulating responses to AZA and mechanisms of resistance (35,113,139,143,144,148). These pathways are tightly interconnected and subject to regulation by epigenetic modifications (163) and miRNAs (164), providing a strong rationale to investigate how AZA+VEN affects their dynamic regulation in leukemic cells.

In our cohort of *BCL2*-mutated responders, AZA+VEN treatment led to notable downregulation of *PLCG2* and myeloid markers *CD11* and *CD14* at cycle 4, alongside upregulation of pro-apoptotic effectors *BIM* and *BAK1*. These results indicate coordinated modulation of PLC signaling, myeloid differentiation, and intrinsic apoptotic pathways, suggesting that BCL2 loss-of-function may rewire signaling networks to enhance sensitivity to the combination therapy. While these findings were obtained in a limited cohort, they support the hypothesis that BCL2 loss-of-function may reconfigure leukemic cells signaling pathways in a way that enhances responsiveness to the combination therapy, potentially via compensatory pathway activation.

To dissect treatment-specific effects independent of *BCL2* status, patients were stratified into Responders and Non-Responders. In the AZA-only group, therapeutic response correlated with early induction of PLC isoforms, myeloid differentiation markers, and pro-apoptotic genes. In contrast, AZA+VEN responders exhibited selective upregulation of *PLCG2* and apoptosis-associated genes, supporting the notion that the two treatments engage overlapping but distinct signaling mechanisms.

To validate these findings under controlled conditions, we used two AML cell lines with distinct therapeutic profiles: MV4-11, a biphenotypic B/myeloid leukemia line harboring FLT3-ITD and MLL-AF4 rearrangements, highly sensitive to both AZA and VEN, and THP-1, a monocytic AML line with MLL-AF9 translocation, responsive to AZA but relatively resistant to VEN. AZA+VEN induced cell cycle arrest in both models, mostly driven by AZA and consistent with its cytostatic effect, while detailed analysis of BCL2 pathways revealed additional regulatory layers beyond gene expression. In MV4-11, AZA+VEN paradoxically increased *BCL2* mRNA but decreased protein levels, suggesting post-transcriptional regulation. Apoptotic induction was confirmed by Annexin V staining, reduced full-length Caspase-3, and accumulation of cleaved PARP, accompanied by upregulation of *BIM* and *BAK1* gene expression. Beyond apoptosis, AZA+VEN selectively modulated PLC/PKC signaling in MV4-11 cells, with decreased PLCG2 protein and increased PKCα phosphorylation, supporting a broader activation of the PKC pathway despite the downregulation of PLCγ2. These changes were absent in VEN-resistant THP-1 cells. This differential regulation translated into lineage-specific differentiation: MV4-11 showed modest upregulation of *CD11b* and *CD14*, indicative of partial monocytic differentiation, whereas THP-1 cells, already partially differentiated at baseline, exhibited stronger induction of *CD11b, CD14*, and *CD33*. This supports the concept that AZA+VEN can simultaneously induce apoptosis and skew differentiation, with the outcome shaped by the baseline signaling architecture and maturation state. Analysis of the AKT/GSK3 axis revealed that AZA-driven suppression of total and phosphorylated AKT occurred in both cell lines, suggesting that AKT downregulation is not the primary determinant of VEN sensitivity. GSK3 isoforms, instead, displayed model-specific modulation: in MV4-11, AZA+VEN reduced GSK3α/β expression and selectively phosphorylated GSK3α, while phosphorylated GSK3β remained undetectable, potentially contributing to apoptosis. In THP-1, GSK3 isoforms were largely unchanged. Given GSK3β role in post-transcriptional networks, including mRNA and miRNA processing, it may also influence key regulators of treatment response in MDS/AML (165).

Collectively, these data indicate that AZA+VEN elicits a multilayered anti-leukemic response, integrating transcriptional, post-transcriptional, and signaling-level changes. These observations underscore that therapeutic response encompasses both apoptosis and functional reprogramming, while highlighting that resistance likely arises from complex adaptive networks. Future studies, including generation of resistant cell lines or introduction of the *BCL2* frameshift mutation into isogenic models, will be critical to dissect adaptive mechanisms and identify novel vulnerabilities exploitable for therapeutic intervention. In addition, larger patient cohorts and integration of multi-omic data will help define robust biomarkers of response and resistance, while investigation of distinct hematopoietic and leukemic subpopulations will clarify differential sensitivity to AZA+VEN.

The functional interplay between phosphoinositide signaling and BCL2-regulated apoptosis also remains a critical area for mechanistic dissection. In conclusion, our findings support a model in which AZA+VEN therapy activates distinct and converging apoptotic and signaling networks, shaped by transcriptional, post-transcriptional, and cell type–specific factors. These results lay the groundwork for future studies aimed at defining biomarkers of response and resistance and provide a mechanistic rationale for personalized therapeutic strategies in high-risk MDS and AML.

Building on these insights, the second aim of this project was to investigate the role of PDZD2 in normal hematopoiesis by establishing a robust CRISPR-Cas9 genome editing platform in HEK293 cells. PDZD2, a poorly characterized gene hypermethylated in nearly 90% of AML cases, was selected as a candidate epigenetic regulator. To this end, a precise genome editing strategy was developed and optimized at the University of Miami in the laboratory of Dr. Figueroa. This platform enables targeted modifications of the *PDZD2* locus, providing a foundation to explore how this factor may influence normal human hematopoiesis.

Using this approach, we engineered defined modifications at the *PDZD2* locus, including an N-terminal HA epitope tag to circumvent the lack of validated antibodies for Western blotting, ChIP, and related applications, a point mutation at the canonical CASP3 cleavage site, and targeted alterations of the NLS signal. The workflow was optimized to maximize HDR efficiency and minimize off-target effects, combining careful sgRNA selection via the Alt-R™ CRISPR HDR Design Tool with NOC-mediated cell cycle synchronization of HEK293 cells.

HEK293 cells were chosen as a model system because, although our ultimate goal was to study PDZD2 in normal hematopoiesis, particularly within the erythroid lineage (51), hematopoietic cells such as HUDEP-2 are challenging to genetically engineer. HEK293 cells provided a tractable platform to introduce precise modifications and characterize the molecular, structural, and functional properties of PDZD2—including expression patterns, subcellular localization, and interacting partners—before translating these findings into more physiologically relevant hematopoietic models.

Cell cycle analysis confirmed effective synchronization with NOC treatment, redistributing cells predominantly into G2-M phase, which is known to favor HDR. This step proved crucial, as the baseline cell cycle distribution in untreated HEK293 cells displayed only a minor fraction of cells in G2-M, limiting the probability of precise KI events. Interestingly, while the literature generally recommends a 1-hour release following NOC treatment to allow cells to progress into G1 before electroporation (166,167), we observed that including this release period actually reduced HDR efficiency. In contrast, electroporation immediately after NOC treatment resulted in higher KI rates. Following electroporation with RNP complexes and HDR donor templates, targeted sequencing of pooled cells revealed differential editing efficiencies among the three loci. The CASP3 site exhibited a relatively high KI rate (~13%), whereas the HA-tag construct showed a markedly lower efficiency (~2%). In contrast, the NLS locus, which required a larger modification, proved more challenging to edit. To facilitate efficient cleavage, two independent sgRNAs were employed to generate a double-strand break across the extended NLS target region. Despite this strategy, the locus displayed a high frequency of indels (~94%), indicating that Cas9 efficiently induced breaks but predominantly engaged error-prone repair pathways. These results underscore the intrinsic variability of CRISPR-Cas9 editing outcomes, influenced by locus-specific chromatin context, target sequence, and repair pathway dynamics, as well as by the size and complexity of the intended modification.

Clonal expansion further confirmed the stability of edits at the CASP3 locus, with two clones achieving complete biallelic KI and several additional clones exhibiting high heterozygous KI efficiencies (69–75%). In contrast, attempts to sequentially introduce the HA tag in pre-edited CASP3 clones were largely unsuccessful, with only minimal KI detected in the non-targeting control clone and no successful integration in CASP3-edited clones. Moreover, prolonged culture of HA KI pools resulted in complete loss of the modification, suggesting limited cellular tolerance or selective disadvantage associated with HA integration at this locus.

Collectively, these findings demonstrate the technical feasibility of introducing precise PDZD2 edits using CRISPR-Cas9 while also revealing significant locus-dependent variability and challenges in sequential editing strategies. The successful generation of CASP3-mutant clones establishes a reliable platform for downstream functional studies, whereas the low efficiency and instability observed for HA-tag insertion and NLS modification underscore the need for careful optimization of donor design, delivery methods, and clonal selection. Overall, this work provides a foundational framework for future genome-editing experiments targeting PDZD2 and other epigenetically regulated loci, enabling targeted functional studies in physiologically relevant contexts and facilitating the exploration of adaptive pathways as well as validation of candidate regulators.

Taken together, these two complementary projects converge toward a common goal: elucidating the molecular circuits that govern leukemic progression and therapeutic response. While the study of AZA+VEN revealed adaptive signaling networks with direct clinical implications, the PDZD2 genome-editing platform establishes a tractable model to interrogate epigenetic regulators in hematopoiesis. Together, they provide a framework that bridges mechanistic insights with innovative experimental tools, ultimately advancing our understanding of MDS and AML biology.

6. REFERENCES

1. Rieger MA, Schroeder T. Hematopoiesis. Cold Spring Harb Perspect Biol. 2012;4:a008250.

2. Palis J. Hematopoietic stem cell-independent hematopoiesis: emergence of erythroid, megakaryocyte, and myeloid potential in the mammalian embryo. FEBS Lett. 2016;590:3965–74.

3. Canu G, Ruhrberg C. First blood: the endothelial origins of hematopoietic progenitors. Angiogenesis. 2021;24:199–211.

4. Yamane T. Cellular Basis of Embryonic Hematopoiesis and Its Implications in Prenatal Erythropoiesis. Int J Mol Sci. 2020;21:9346.

5. Klaus A, Robin C. Embryonic hematopoiesis under microscopic observation. Dev Biol. 2017;428:318–27.

6. Belyavsky A, Petinati N, Drize N. Hematopoiesis during Ontogenesis, Adult Life, and Aging. Int J Mol Sci. 2021;22:9231.

7. Kumar A, D’Souza SS, Thakur AS. Understanding the Journey of Human Hematopoietic Stem Cell Development. Stem Cells Int. 2019;2019:2141475.

8. Zhang Y, Liu F. The evolving views of hematopoiesis: from embryo to adulthood and from in vivo to in vitro. J Genet Genomics. 2024;51:3–15.

9. Orfao A, Matarraz S, Pérez-Andrés M, Almeida J, Teodosio C, Berkowska MA, et al. Immunophenotypic dissection of normal hematopoiesis. J Immunol Methods. 2019;475:112684.

10. Liu J, Tong J, Yang H. Targeting CD33 for acute myeloid leukemia therapy. BMC Cancer. 2022;22:24.

11. Wu Z, Zhang Z, Lei Z, Lei P. CD14: Biology and role in the pathogenesis of disease. Cytokine Growth Factor Rev. 2019;48:24–31.

12. Tucker J, Dorey E, Gregory WM, Simpson AP, Amess JA, Lister TA, et al. Immunophenotype of blast cells in acute myeloid leukemia may be a useful predictive factor for outcome. Hematol Oncol. 1990;8:47–58.

13. Tien HF, Wang CH, Lin MT, Lee FY, Liu MC, Chuang SM, et al. Correlation of cytogenetic results with immunophenotype, genotype, clinical features, and ras mutation in acute myeloid leukemia. A study of 235 Chinese patients in Taiwan. Cancer Genet Cytogenet. 1995;84:60–8.

14. Hasserjian RP, Germing U, Malcovati L. Diagnosis and classification of myelodysplastic syndromes. Blood. 2023;142:2247–57.

15. Maggioni G, Della Porta MG. Molecular landscape of myelodysplastic neoplasms in disease classification and prognostication. Curr Opin Hematol. 2023;30:30–7.

16. Greenberg PL, Tuechler H, Schanz J, Sanz G, Garcia-Manero G, Solé F, et al. Revised international prognostic scoring system for myelodysplastic syndromes. Blood. 2012;120:2454–65.

17. Sekeres MA, Taylor J. Diagnosis and Treatment of Myelodysplastic Syndromes: A Review. JAMA. 2022;328:872–80.

18. Bernard E, Tuechler H, Greenberg PL, Hasserjian RP, Arango Ossa JE, Nannya Y, et al. Molecular International Prognostic Scoring System for Myelodysplastic Syndromes. NEJM Evid. 2022;1:EVIDoa2200008.

19. Kabel AM, Zamzami F, Al-Talhi M, Al-Dwila K, Hamza R. Acute Myeloid Leukemia: A focus on Risk Factors, Clinical Presentation, Diagnosis and Possible Lines of Management. Journal of Cancer Research and Treatment. Science and Education Publishing; 2017;5:62–7.

20. Short NJ, Rytting ME, Cortes JE. Acute myeloid leukaemia. Lancet. 2018;392:593–606.

21. Menssen AJ, Walter MJ. Genetics of progression from MDS to secondary leukemia. Blood. 2020;136:50–60.

22. Cazzola M. Myelodysplastic Syndromes. N Engl J Med. 2020;383:1358–74.

23. Cazzola M, Della Porta MG, Malcovati L. The genetic basis of myelodysplasia and its clinical relevance. Blood. 2013;122:4021–34.

24. Bănescu C, Tripon F, Muntean C. The Genetic Landscape of Myelodysplastic Neoplasm Progression to Acute Myeloid Leukemia. Int J Mol Sci. 2023;24:5734.

25. Nagata Y, Maciejewski JP. The functional mechanisms of mutations in myelodysplastic syndrome. Leukemia. 2019;33:2779–94.

26. Visconte V, O Nakashima M, J Rogers H. Mutations in Splicing Factor Genes in Myeloid Malignancies: Significance and Impact on Clinical Features. Cancers (Basel). 2019;11:1844.

27. Chen S, Benbarche S, Abdel-Wahab O. Splicing factor mutations in hematologic malignancies. Blood. 2021;138:599–612.

28. Pellagatti A, Armstrong RN, Steeples V, Sharma E, Repapi E, Singh S, et al. Impact of spliceosome mutations on RNA splicing in myelodysplasia: dysregulated genes/pathways and clinical associations. Blood. 2018;132:1225–40.

29. Kataoka N, Matsumoto E, Masaki S. Mechanistic Insights of Aberrant Splicing with Splicing Factor Mutations Found in Myelodysplastic Syndromes. Int J Mol Sci. 2021;22:7789.

30. Ogawa S. Genetics of MDS. Blood. 2019;133:1049–59.

31. Huang H-T, Figueroa ME. Epigenetic deregulation in myeloid malignancies. Blood. 2021;138:613–24.

32. Meldi KM, Figueroa ME. Cytosine modifications in myeloid malignancies. Pharmacol Ther. 2015;152:42–53.

33. Meldi KM, Figueroa ME. Epigenetic deregulation in myeloid malignancies. Transl Res. 2015;165:102–14.

34. Jädersten M, Saft L, Smith A, Kulasekararaj A, Pomplun S, Göhring G, et al. TP53 mutations in low-risk myelodysplastic syndromes with del(5q) predict disease progression. J Clin Oncol. 2011;29:1971–9.

35. Follo MY, Pellagatti A, Armstrong RN, Ratti S, Mongiorgi S, De Fanti S, et al. Response of high-risk MDS to azacitidine and lenalidomide is impacted by baseline and acquired mutations in a cluster of three inositide-specific genes. Leukemia. 2019;33:2276–90.

36. Bullinger L, Döhner K, Döhner H. Genomics of Acute Myeloid Leukemia Diagnosis and Pathways. J Clin Oncol. 2017;35:934–46.

37. Casalin I, De Stefano A, Ceneri E, Cappellini A, Finelli C, Curti A, et al. Deciphering signaling pathways in hematopoietic stem cells: the molecular complexity of Myelodysplastic Syndromes (MDS) and leukemic progression. Advances in Biological Regulation. 2024;101014.

38. Figueroa ME, Lugthart S, Li Y, Erpelinck-Verschueren C, Deng X, Christos PJ, et al. DNA methylation signatures identify biologically distinct subtypes in acute myeloid leukemia. Cancer Cell. 2010;17:13–27.

39. Guerrero Schimpf ML, Figueroa ME. The Autocrine Secreted PDZD2 Functions As a Novel Tumor Suppressor in AML, Inducing Growth Inhibition and Cell Cycle Arrest. Blood. 2021;138:3320.

40. Ye F, Zhang M. Structures and target recognition modes of PDZ domains: recurring themes and emerging pictures. Biochem J. 2013;455:1–14.

41. Liu X, Fuentes EJ. Emerging Themes in PDZ Domain Signaling: Structure, Function, and Inhibition. Int Rev Cell Mol Biol. 2019;343:129–218.

42. Manjunath GP, Ramanujam PL, Galande S. Structure function relations in PDZ-domain-containing proteins: Implications for protein networks in cellular signalling. J Biosci. 2018;43:155–71.

43. Sheng M, Sala C. PDZ domains and the organization of supramolecular complexes. Annu Rev Neurosci. 2001;24:1–29.

44. Ernst A, Appleton BA, Ivarsson Y, Zhang Y, Gfeller D, Wiesmann C, et al. A structural portrait of the PDZ domain family. J Mol Biol. 2014;426:3509–19.

45. Lee H-J, Zheng JJ. PDZ domains and their binding partners: structure, specificity, and modification. Cell Commun Signal. 2010;8:8.

46. Yeung M-L, Tam TSM, Tsang ACC, Yao K-M. Proteolytic cleavage of PDZD2 generates a secreted peptide containing two PDZ domains. EMBO Rep. 2003;4:412–8.

47. Subbaiah VK, Kranjec C, Thomas M, Banks L. PDZ domains: the building blocks regulating tumorigenesis. Biochem J. 2011;439:195–205.

48. Facciuto F, Cavatorta AL, Valdano MB, Marziali F, Gardiol D. Differential expression of PDZ domain-containing proteins in human diseases - challenging topics and novel issues. FEBS J. 2012;279:3538–48.

49. Tam CW, Cheng AS, Ma RYM, Yao K-M, Shiu SYW. Inhibition of prostate cancer cell growth by human secreted PDZ domain-containing protein 2, a potential autocrine prostate tumor suppressor. Endocrinology. 2006;147:5023–33.

50. Ma RYM, Tam TSM, Suen APM, Yeung PML, Tsang SW, Chung SK, et al. Secreted PDZD2 exerts concentration-dependent effects on the proliferation of INS-1E cells. Int J Biochem Cell Biol. 2006;38:1015–22.

51. Guerrero Schimpf ML, Pannullo MS, Sparger CC, Huang H-T, Wade DL, Figueroa MKE. PDZD2 Is Required for Normal Erythropoiesis and Its 37-KDa Secreted Product, sPDZD2, Functions As a Soluble Tumor Suppressor in AML. Blood. 2023;142:2679.

52. Hellström-Lindberg ES, Kröger N. Clinical decision-making and treatment of myelodysplastic syndromes. Blood. 2023;142:2268–81.

53. Sorrentino VG, Thota S, Gonzalez EA, Rameshwar P, Chang VT, Etchegaray J-P. Hypomethylating Chemotherapeutic Agents as Therapy for Myelodysplastic Syndromes and Prevention of Acute Myeloid Leukemia. Pharmaceuticals (Basel). 2021;14:641.

54. Duchmann M, Itzykson R. Clinical update on hypomethylating agents. Int J Hematol. 2019;110:161–9.

55. Raj K, Mufti GJ. Azacytidine (Vidaza(R)) in the treatment of myelodysplastic syndromes. Ther Clin Risk Manag. 2006;2:377–88.

56. Bazinet A, Bravo GM. New Approaches to Myelodysplastic Syndrome Treatment. Curr Treat Options Oncol. 2022;23:668–87.

57. Choi JH, Shukla M, Abdul-Hay M. Acute Myeloid Leukemia Treatment in the Elderly: A Comprehensive Review of the Present and Future. Acta Haematol. 2023;146:431–57.

58. Diesch J, Zwick A, Garz A-K, Palau A, Buschbeck M, Götze KS. A clinical-molecular update on azanucleoside-based therapy for the treatment of hematologic cancers. Clin Epigenetics. 2016;8:71.

59. Blum S, Tsilimidos G, Bresser H, Lübbert M. Role of Bcl-2 inhibition in myelodysplastic syndromes. Int J Cancer. 2023;152:1526–35.

60. Garcia JS. Prospects for Venetoclax in Myelodysplastic Syndromes. Hematol Oncol Clin North Am. 2020;34:441–8.

61. Garciaz S, Saillard C, Hicheri Y, Hospital M-A, Vey N. Venetoclax in Acute Myeloid Leukemia: Molecular Basis, Evidences for Preclinical and Clinical Efficacy and Strategies to Target Resistance. Cancers (Basel). 2021;13:5608.

62. Ashkenazi A, Fairbrother WJ, Leverson JD, Souers AJ. From basic apoptosis discoveries to advanced selective BCL-2 family inhibitors. Nat Rev Drug Discov. 2017;16:273–84.

63. Liu J, Chen Y, Yu L, Yang L. Mechanisms of venetoclax resistance and solutions. Front Oncol. 2022;12:1005659.

64. Tahir SK, Smith ML, Hessler P, Rapp LR, Idler KB, Park CH, et al. Potential mechanisms of resistance to venetoclax and strategies to circumvent it. BMC Cancer. 2017;17:399.

65. Zeidan AM, Borate U, Pollyea DA, Brunner AM, Roncolato F, Garcia JS, et al. A phase 1b study of venetoclax and azacitidine combination in patients with relapsed or refractory myelodysplastic syndromes. Am J Hematol. 2023;98:272–81.

66. Braish JS, Montalban-Bravo G, Ravandi F, Short N, Kadia T, Ohanian M, et al. Safety and efficacy of the combination of azacitidine with venetoclax after hypomethylating agent failure in higher-risk myelodysplastic syndrome. Leuk Res. 2025;153:107692.

67. Zeidan AM, Garcia JS, Fenaux P, Platzbecker U, Miyazaki Y, Xiao Z-J, et al. Phase 3 VERONA study of venetoclax with azacitidine to assess change in complete remission and overall survival in treatment-naïve higher-risk myelodysplastic syndromes. JCO. Wolters Kluwer; 2021;39:TPS7054–TPS7054.

68. Pollyea DA, Stevens BM, Jones CL, Winters A, Pei S, Minhajuddin M, et al. Venetoclax with azacitidine disrupts energy metabolism and targets leukemia stem cells in patients with acute myeloid leukemia. Nat Med. 2018;24:1859–66.

69. Bogenberger JM, Kornblau SM, Pierceall WE, Lena R, Chow D, Shi C-X, et al. BCL-2 family proteins as 5-Azacytidine-sensitizing targets and determinants of response in myeloid malignancies. Leukemia. 2014;28:1657–65.

70. Jin S, Cojocari D, Purkal JJ, Popovic R, Talaty NN, Xiao Y, et al. 5-Azacitidine Induces NOXA to Prime AML Cells for Venetoclax-Mediated Apoptosis. Clin Cancer Res. 2020;26:3371–83.

71. Mishra R, Zokaei Nikoo M, Veeraballi S, Singh A. Venetoclax and Hypomethylating Agent Combination in Myeloid Malignancies: Mechanisms of Synergy and Challenges of Resistance. Int J Mol Sci. 2023;25:484.

72. Lee JB, Khan DH, Hurren R, Xu M, Na Y, Kang H, et al. Venetoclax enhances T cell-mediated antileukemic activity by increasing ROS production. Blood. 2021;138:234–45.

73. Zhang Q, Riley-Gillis B, Han L, Jia Y, Lodi A, Zhang H, et al. Activation of RAS/MAPK pathway confers MCL-1 mediated acquired resistance to BCL-2 inhibitor venetoclax in acute myeloid leukemia. Signal Transduct Target Ther. 2022;7:51.

74. Estaquier J, Vallette F, Vayssiere J-L, Mignotte B. The mitochondrial pathways of apoptosis. Adv Exp Med Biol. 2012;942:157–83.

75. Czabotar PE, Garcia-Saez AJ. Mechanisms of BCL-2 family proteins in mitochondrial apoptosis. Nat Rev Mol Cell Biol. 2023;24:732–48.

76. Dadsena S, King LE, García-Sáez AJ. Apoptosis regulation at the mitochondria membrane level. Biochim Biophys Acta Biomembr. 2021;1863:183716.

77. Murphy E, Ardehali H, Balaban RS, DiLisa F, Dorn GW, Kitsis RN, et al. Mitochondrial Function, Biology, and Role in Disease: A Scientific Statement From the American Heart Association. Circ Res. 2016;118:1960–91.

78. Jiang X, Jiang H, Shen Z, Wang X. Activation of mitochondrial protease OMA1 by Bax and Bak promotes cytochrome c release during apoptosis. Proc Natl Acad Sci U S A. 2014;111:14782–7.

79. Kalkavan H, Green DR. MOMP, cell suicide as a BCL-2 family business. Cell Death Differ. 2018;25:46–55.

80. Wolf P, Schoeniger A, Edlich F. Pro-apoptotic complexes of BAX and BAK on the outer mitochondrial membrane. Biochim Biophys Acta Mol Cell Res. 2022;1869:119317.

81. Sekar G, Ojoawo A, Moldoveanu T. Protein-protein and protein-lipid interactions of pore-forming BCL-2 family proteins in apoptosis initiation. Biochem Soc Trans. 2022;50:1091–103.

82. Willis SN, Adams JM. Life in the balance: how BH3-only proteins induce apoptosis. Curr Opin Cell Biol. 2005;17:617–25.

83. López-Royuela N, Pérez-Galán P, Galán-Malo P, Yuste VJ, Anel A, Susín SA, et al. Different contribution of BH3-only proteins and caspases to doxorubicin-induced apoptosis in p53-deficient leukemia cells. Biochem Pharmacol. 2010;79:1746–58.

84. Dai H, Ding H, Meng XW, Peterson KL, Schneider PA, Karp JE, et al. Constitutive BAK activation as a determinant of drug sensitivity in malignant lymphohematopoietic cells. Genes Dev. 2015;29:2140–52.

85. King LE, Hohorst L, García-Sáez AJ. Expanding roles of BCL-2 proteins in apoptosis execution and beyond. J Cell Sci. 2023;136:jcs260790.

86. Xian J, Owusu Obeng E, Ratti S, Rusciano I, Marvi MV, Fazio A, et al. Nuclear Inositides and Inositide-Dependent Signaling Pathways in Myelodysplastic Syndromes. Cells. 2020;9:697.

87. Posor Y, Jang W, Haucke V. Phosphoinositides as membrane organizers. Nat Rev Mol Cell Biol. 2022;23:797–816.

88. Schink KO, Tan K-W, Stenmark H. Phosphoinositides in Control of Membrane Dynamics. Annu Rev Cell Dev Biol. 2016;32:143–71.

89. Dickson EJ, Hille B. Understanding phosphoinositides: rare, dynamic, and essential membrane phospholipids. Biochem J. 2019;476:1–23.

90. Fiume R, Faenza I, Sheth B, Poli A, Vidalle MC, Mazzetti C, et al. Nuclear Phosphoinositides: Their Regulation and Roles in Nuclear Functions. Int J Mol Sci. 2019;20:2991.

91. Vidalle MC, Sheth B, Fazio A, Marvi MV, Leto S, Koufi F-D, et al. Nuclear Phosphoinositides as Key Determinants of Nuclear Functions. Biomolecules. Multidisciplinary Digital Publishing Institute; 2023;13:1049.

92. Davies EM, Mitchell CA, Stenmark HA. Phosphoinositides in New Spaces. Cold Spring Harb Perspect Biol. 2023;15:a041406.

93. Balla T. Phosphoinositides: tiny lipids with giant impact on cell regulation. Physiol Rev. 2013;93:1019–137.

94. Davies EM, Jones EI, Ooms LM, Gurung R, McGrath MJ, Mitchell CA. Phosphoinositide phosphatases: Modifiers of phosphoinositide signaling in health and disease. Biochim Biophys Acta Mol Cell Biol Lipids. 2025;1870:159652.

95. Kielkowska A, Niewczas I, Anderson KE, Durrant TN, Clark J, Stephens LR, et al. A new approach to measuring phosphoinositides in cells by mass spectrometry. Advances in Biological Regulation. 2014;54:131–41.

96. Kanemaru K, Nakamura Y. Activation Mechanisms and Diverse Functions of Mammalian Phospholipase C. Biomolecules. 2023;13:915.

97. Katan M, Cockcroft S. Phospholipase C families: Common themes and versatility in physiology and pathology. Prog Lipid Res. 2020;80:101065.

98. Kadamur G, Ross EM. Mammalian phospholipase C. Annu Rev Physiol. 2013;75:127–54.

99. Gresset A, Sondek J, Harden TK. The phospholipase C isozymes and their regulation. Subcell Biochem. 2012;58:61–94.

100. Senarath K, Fisher IJ, Jang W, Lu S, Inoue A, Kostenis E, et al. An integrated mechanism of Gq regulation of PLCβ enzymes. Proc Natl Acad Sci U S A. 2025;122:e2500318122.

101. Nakamura Y, Fukami K. Regulation and physiological functions of mammalian phospholipase C. J Biochem. 2017;161:315–21.

102. Ratti S, Mongiorgi S, Ramazzotti G, Follo MY, Mariani GA, Suh P-G, et al. Nuclear Inositide Signaling Via Phospholipase C. J Cell Biochem. 2017;118:1969–78.

103. Martelli AM, Follo MY, Evangelisti C, Falà F, Fiume R, Billi AM, et al. Nuclear inositol lipid metabolism: more than just second messenger generation? J Cell Biochem. 2005;96:285–92.

104. Yang YR, Follo MY, Cocco L, Suh P-G. The physiological roles of primary phospholipase C. Adv Biol Regul. 2013;53:232–41.

105. Peruzzi D, Aluigi M, Manzoli L, Billi AM, Di Giorgio FP, Morleo M, et al. Molecular characterization of the human PLC beta1 gene. Biochim Biophys Acta. 2002;1584:46–54.

106. Ramazzotti G, Fiume R, Chiarini F, Campana G, Ratti S, Billi AM, et al. Phospholipase C-β1 interacts with cyclin E in adipose- derived stem cells osteogenic differentiation. Adv Biol Regul. 2019;71:1–9.

107. Mongiorgi S, Follo MY, Yang YR, Ratti S, Manzoli L, McCubrey JA, et al. Selective Activation of Nuclear PI-PLCbeta1 During Normal and Therapy-Related Differentiation. Curr Pharm Des. 2016;22:2345–8.

108. Cocco L, Manzoli L, Faenza I, Ramazzotti G, Yang YR, McCubrey JA, et al. Modulation of nuclear PI-PLCbeta1 during cell differentiation. Adv Biol Regul. 2016;60:1–5.

109. Casalin I, Ceneri E, Ratti S, Manzoli L, Cocco L, Follo MY. Nuclear Phospholipids and Signaling: An Update of the Story. Cells. 2024;13:713.

110. Follo MY, Finelli C, Clissa C, Mongiorgi S, Bosi C, Martinelli G, et al. Phosphoinositide-phospholipase C beta1 mono-allelic deletion is associated with myelodysplastic syndromes evolution into acute myeloid leukemia. J Clin Oncol. 2009;27:782–90.

111. Lo Vasco VR, Calabrese G, Manzoli L, Palka G, Spadano A, Morizio E, et al. Inositide-specific phospholipase c beta1 gene deletion in the progression of myelodysplastic syndrome to acute myeloid leukemia. Leukemia. 2004;18:1122–6.

112. Cocco L, Finelli C, Mongiorgi S, Clissa C, Russo D, Bosi C, et al. An increased expression of PI-PLCβ1 is associated with myeloid differentiation and a longer response to azacitidine in myelodysplastic syndromes. J Leukoc Biol. 2015;98:769–80.

113. Follo MY, Finelli C, Mongiorgi S, Clissa C, Bosi C, Testoni N, et al. Reduction of phosphoinositide-phospholipase C beta1 methylation predicts the responsiveness to azacitidine in high-risk MDS. Proceedings of the National Academy of Sciences of the United States of America. National Academy of Sciences; 2009;106:16811.

114. Follo MY, Finelli C, Mongiorgi S, Clissa C, Chiarini F, Ramazzotti G, et al. Synergistic induction of PI-PLCβ1 signaling by azacitidine and valproic acid in high-risk myelodysplastic syndromes. Leukemia. 2011;25:271–80.

115. Follo MY, Russo D, Finelli C, Mongiorgi S, Clissa C, Filì C, et al. Epigenetic regulation of nuclear PI-PLCbeta1 signaling pathway in low-risk MDS patients during azacitidine treatment. Leukemia. 2012;26:943–50.

116. Rhee SG, Bae YS. Regulation of phosphoinositide-specific phospholipase C isozymes. J Biol Chem. 1997;272:15045–8.

117. Lattanzio R, Piantelli M, Falasca M. Role of phospholipase C in cell invasion and metastasis. Adv Biol Regul. 2013;53:309–18.

118. Jackson JT, Mulazzani E, Nutt SL, Masters SL. The role of PLCγ2 in immunological disorders, cancer, and neurodegeneration. J Biol Chem. 2021;297:100905.

119. Fukami K, Inanobe S, Kanemaru K, Nakamura Y. Phospholipase C is a key enzyme regulating intracellular calcium and modulating the phosphoinositide balance. Prog Lipid Res. 2010;49:429–37.

120. Nishizuka Y. Intracellular signaling by hydrolysis of phospholipids and activation of protein kinase C. Science. 1992;258:607–14.

121. Miranda MB, Johnson DE. Signal transduction pathways that contribute to myeloid differentiation. Leukemia. 2007;21:1363–77.

122. Barbosa CMV, Bincoletto C, Barros CC, Ferreira AT, Paredes-Gamero EJ. PLCγ2 and PKC are important to myeloid lineage commitment triggered by M-SCF and G-CSF. J Cell Biochem. 2014;115:42–51.

123. Mogami H, Zhang H, Suzuki Y, Urano T, Saito N, Kojima I, et al. Decoding of short-lived Ca2+ influx signals into long term substrate phosphorylation through activation of two distinct classes of protein kinase C. J Biol Chem. 2003;278:9896–904.

124. Oancea E, Meyer T. Protein kinase C as a molecular machine for decoding calcium and diacylglycerol signals. Cell. 1998;95:307–18.

125. Wuttke A, Yu Q, Tengholm A. Autocrine Signaling Underlies Fast Repetitive Plasma Membrane Translocation of Conventional and Novel Protein Kinase C Isoforms in β Cells. J Biol Chem. 2016;291:14986–95.

126. Kawano T, Inokuchi J, Eto M, Murata M, Kang J-H. Protein Kinase C (PKC) Isozymes as Diagnostic and Prognostic Biomarkers and Therapeutic Targets for Cancer. Cancers (Basel). 2022;14:5425.

127. Altman A, Kong K-F. Protein Kinase C Enzymes in the Hematopoietic and Immune Systems. Annu Rev Immunol. 2016;34:511–38.

128. Takami M, Katayama K, Noguchi K, Sugimoto Y. Protein kinase C alpha-mediated phosphorylation of PIM-1L promotes the survival and proliferation of acute myeloid leukemia cells. Biochem Biophys Res Commun. 2018;503:1364–71.

129. Poli A, Ratti S, Finelli C, Mongiorgi S, Clissa C, Lonetti A, et al. Nuclear translocation of PKC-α is associated with cell cycle arrest and erythroid differentiation in myelodysplastic syndromes (MDSs). FASEB J. 2018;32:681–92.

130. Black AR, Black JD. The complexities of PKCα signaling in cancer. Adv Biol Regul. 2021;80:100769.

131. Engelman JA, Luo J, Cantley LC. The evolution of phosphatidylinositol 3-kinases as regulators of growth and metabolism. Nat Rev Genet. 2006;7:606–19.

132. Follo MY, Mongiorgi S, Bosi C, Cappellini A, Finelli C, Chiarini F, et al. The AKT/mammalian target of rapamycin signal transduction pathway is activated in high-risk myelodysplastic syndromes and influences cell survival and proliferation. Cancer Res. 2007;67:4287–94.

133. Shaw AL, Burke JE. Molecular insight on the role of the phosphoinositide PIP3 in regulating the protein kinases AKT, PDK1, and BTK. Biochem Soc Trans. 2025;53:737–49.

134. Duronio V. The life of a cell: apoptosis regulation by the PI3K/PKB pathway. Biochem J. 2008;415:333–44.

135. Coffer PJ, Jin J, Woodgett JR. Protein kinase B (c-AKT): a multifunctional mediator of phosphatidylinositol 3-kinase activation. Biochem J. 1998;335 (Pt 1):1–13.

136. Hermida MA, Dinesh Kumar J, Leslie NR. GSK3 and its interactions with the PI3K/AKT/mTOR signalling network. Adv Biol Regul. 2017;65:5–15.

137. Datta SR, Dudek H, Tao X, Masters S, Fu H, Gotoh Y, et al. AKT phosphorylation of BAD couples survival signals to the cell-intrinsic death machinery. Cell. 1997;91:231–41.

138. Goode N, Hughes K, Woodgett JR, Parker PJ. Differential regulation of glycogen synthase kinase-3 beta by protein kinase C isotypes. Journal of Biological Chemistry. 1992;267:16878–82.

139. Ratti S, Mongiorgi S, Rusciano I, Manzoli L, Follo MY. Glycogen Synthase Kinase-3 and phospholipase C-beta signalling: Roles and possible interactions in myelodysplastic syndromes and acute myeloid leukemia. Biochim Biophys Acta Mol Cell Res. 2020;1867:118649.

140. Beurel E, Grieco SF, Jope RS. Glycogen synthase kinase-3 (GSK3): regulation, actions, and diseases. Pharmacol Ther. 2015;148:114–31.

141. Huang J, Zhang Y, Bersenev A, O'Brien WT, Tong W, Emerson SG, et al. Pivotal role for glycogen synthase kinase-3 in hematopoietic stem cell homeostasis in mice. J Clin Invest. 2009;119:3519–29.

142. Trowbridge JJ, Xenocostas A, Moon RT, Bhatia M. Glycogen synthase kinase-3 is an in vivo regulator of hematopoietic stem cell repopulation. Nat Med. 2006;12:89–98.

143. Guezguez B, Almakadi M, Benoit YD, Shapovalova Z, Rahmig S, Fiebig-Comyn A, et al. GSK3 Deficiencies in Hematopoietic Stem Cells Initiate Pre-neoplastic State that Is Predictive of Clinical Outcomes of Human Acute Leukemia. Cancer Cell. 2016;29:61–74.

144. Martelli AM, Evangelisti C, Paganelli F, Chiarini F, McCubrey JA. GSK-3: a multifaceted player in acute leukemias. Leukemia. 2021;35:1829–42.

145. Banerji V, Frumm SM, Ross KN, Li LS, Schinzel AC, Hahn CK, et al. The intersection of genetic and chemical genomic screens identifies GSK-3α as a target in human acute myeloid leukemia. J Clin Invest. 2012;122:935–47.

146. Mudgapalli N, Nallasamy P, Chava H, Chava S, Pathania AS, Gunda V, et al. The role of exosomes and MYC in therapy resistance of acute myeloid leukemia: Challenges and opportunities. Mol Aspects Med. 2019;70:21–32.

147. Ignatz-Hoover JJ, Wang V, Mackowski NM, Roe AJ, Ghansah IK, Ueda M, et al. Aberrant GSK3β nuclear localization promotes AML growth and drug resistance. Blood Adv. 2018;2:2890–903.

148. Ricciardi MR, Mirabilii S, Licchetta R, Piedimonte M, Tafuri A. Targeting the AKT, GSK-3, Bcl-2 axis in acute myeloid leukemia. Adv Biol Regul. 2017;65:36–58.

149. Zhang Y, Xia F, Liu X, Yu Z, Xie L, Liu L, et al. JAM3 maintains leukemia-initiating cell self-renewal through LRP5/AKT/β-catenin/CCND1 signaling. J Clin Invest. 2018;128:1737–51.

150. McCubrey JA, Fitzgerald TL, Yang LV, Lertpiriyapong K, Steelman LS, Abrams SL, et al. Roles of GSK-3 and microRNAs on epithelial mesenchymal transition and cancer stem cells. Oncotarget. Impact Journals; 2016;8:14221–50.

151. Ferrari A, Arniani S, Crescenzi B, Ascani S, Flenghi L, Pierini V, et al. High grade B-cell lymphoma with MYC, BCL2 and/or BCL6 rearrangements: unraveling the genetic landscape of a rare aggressive subtype of non-Hodgkin lymphoma. Leukemia & Lymphoma. Taylor & Francis; 2022;63:1356–62.

152. Hong M, He G. The 2016 Revision to the World Health Organization Classification of Myelodysplastic Syndromes. J Transl Int Med. 2017;5:139–43.

153. Sorenson CM. Bcl-2 family members and disease. Biochimica et Biophysica Acta (BBA) - Molecular Cell Research. 2004;1644:169–77.

154. Carter JL, Su Y, Qiao X, Zhao J, Wang G, Howard M, et al. Acquired resistance to venetoclax plus azacitidine in acute myeloid leukemia: In vitro models and mechanisms. Biochem Pharmacol. 2023;216:115759.

155. Los M, Mozoluk M, Ferrari D, Stepczynska A, Stroh C, Renz A, et al. Activation and Caspase-mediated Inhibition of PARP: A Molecular Switch between Fibroblast Necrosis and Apoptosis in Death Receptor Signaling. Mol Biol Cell. 2002;13:978–88.

156. Alimandi M, Heidaran MA, Gutkind JS, Zhang J, Ellmore N, Valius M, et al. PLC-γ activation is required for PDGF-βR-mediated mitogenesis and monocytic differentiation of myeloid progenitor cells. Oncogene. Nature Publishing Group; 1997;15:585–93.

157. Bazinet A, Desikan SP, Li Z, Rodriguez-Sevilla JJ, Venugopal S, Urrutia S, et al. Cytogenetic and Molecular Associations with Outcomes in Higher-Risk Myelodysplastic Syndromes Treated with Hypomethylating Agents plus Venetoclax. Clin Cancer Res. 2024;30:1319–26.

158. Ikoma Y, Nakamura N, Kaneda Y, Takamori H, Seki T, Hiramoto N, et al. Impact of myelodysplasia-related gene mutations and residual mutations at remission in venetoclax/azacitidine for AML. Leukemia. 2025;39:1362–7.

159. Moujalled DM, Brown FC, Chua CC, Dengler MA, Pomilio G, Anstee NS, et al. Acquired mutations in BAX confer resistance to BH3-mimetic therapy in acute myeloid leukemia. Blood. 2023;141:634–44.

160. Garciaz S, Hospital M-A, Collette Y, Vey N. Venetoclax Resistance in Acute Myeloid Leukemia. Cancers (Basel). 2024;16:1091.

161. Blombery P, Anderson MA, Gong J-N, Thijssen R, Birkinshaw RW, Thompson ER, et al. Acquisition of the Recurrent Gly101Val Mutation in BCL2 Confers Resistance to Venetoclax in Patients with Progressive Chronic Lymphocytic Leukemia. Cancer Discov. 2019;9:342–53.

162. DiNardo CD, Jonas BA, Pullarkat V, Thirman MJ, Garcia JS, Wei AH, et al. Azacitidine and Venetoclax in Previously Untreated Acute Myeloid Leukemia. N Engl J Med. 2020;383:617–29.

163. Mongiorgi S, Finelli C, Yang YR, Clissa C, McCubrey JA, Billi AM, et al. Inositide-dependent signaling pathways as new therapeutic targets in myelodysplastic syndromes. Expert Opin Ther Targets. 2016;20:677–87.

164. Mongiorgi S, De Stefano A, Ratti S, Indio V, Astolfi A, Casalin I, et al. A miRNA screening identifies miR-192-5p as associated with response to azacitidine and lenalidomide therapy in myelodysplastic syndromes. Clin Epigenetics. 2023;15:27.

165. Duda P, Akula SM, Abrams SL, Steelman LS, Gizak A, Rakus D, et al. GSK-3 and miRs: Master regulators of therapeutic sensitivity of cancer cells. Biochim Biophys Acta Mol Cell Res. 2020;1867:118770.

166. Surani AA, Colombo SL, Barlow G, Foulds GA, Montiel-Duarte C. Optimizing Cell Synchronization Using Nocodazole or Double Thymidine Block. Methods Mol Biol. 2021;2329:111–21.

167. Choi HJ, Fukui M, Zhu BT. Role of cyclin B1/Cdc2 up-regulation in the development of mitotic prometaphase arrest in human breast cancer cells treated with nocodazole. PLoS One. 2011;6:e24312.

7. ACKNOWLEDGEMENTS

I would like to sincerely thank the entire Anatomy Group at the University of Bologna, Department of Biomedical and Neuromotor Sciences, directed by Prof. Lucia Manzoli and Prof. Stefano Ratti, for their constant support throughout my research activities. I am especially grateful to Prof. Lucio Cocco for his encouragement and guidance during my PhD journey.

My deepest gratitude goes to my supervisor, Prof. Matilde Follo, for her invaluable mentorship, continuous guidance, and support in research planning and thesis writing.

I am also thankful to the Institute of Hematology "L. and A. Seragnoli" of the Policlinico S. Orsola in Bologna, and in particular to Dr. Antonio Curti and Dr. Carlo Finelli, for their collaborative spirit in carrying out the study. I further acknowledge the Laboratory of Biosciences at the Istituto Romagnolo per lo Studio e la Cura dei Tumori (IRST) "Dino Amadori" in Meldola, with special thanks to Dr. Anna Ferrari, Dr. Giorgia Simonetti, and Prof. Giovanni Martinelli, for their valuable contributions to this project.

Finally, I am deeply grateful to the Figueroa Lab at the University of Miami. In particular, I wish to thank Dr. Maria Figueroa for her support during my research period in Miami, Dr. Marlise Guerrero-Schimpf for her assistance with the experiments, and all the lab members for everything they taught me and for making my experience so enriching.